Aileen Sauermoser, BSc
01230547

Perylenediimide Derivatives as Acceptor Material for Organic Photovoltaics

MASTER THESIS

In partial fulfillment of the requirements for the academic degree
Diplom-Ingenieur
in the field of study of Technical Chemistry

submitted at
Graz University of Technology

Under the supervision of
Univ.-Prof. Dipl.-Ing. Dr.techn. Gregor Trimmel
Institute for Chemistry and Technology of Materials

Graz, January 2020

Affidavit / Eidesstattliche Erklärung

I declare that I have authored this thesis independently, that I have not used other than the declared sources/resources, and that I have explicitly indicated all material which has been quoted either literally or by content from the sources used. The text document uploaded to TUGRAZonline is identical to the present master's thesis.

Ich erkläre an Eides statt, dass ich die vorliegende Arbeit selbstständig verfasst, andere als die angegebenen Quellen/Hilfsmittel nicht benutzt, und die in den benutzten Quellen wörtlich und inhaltlich entnommenen Stellen als solche kenntlich gemacht habe. Das in TUGRAZonline hochgeladene Textdokument ist mit der vorliegenden Masterarbeit identisch.

_____ _____

Date/Datum Signature/Unterschrift

The scientist is not a person who gives the right answers, he's one who asks the right questions.

-- Claude Levi-Strauss

Abstract

Renewable energies are one of the most important energy sources, due the increasing energy demand and the amount of pollution due to fossil fuels. Therefore, photovoltaic systems are a key factor to replace conventional energy sources.

Solar cells can be produced out of different materials such as inorganic, organic, polymeric ones, as well as hybrids. Since crystalline silicon based solar cells are quite expensive when it comes to manufacturing processes, research is done on cheaper and easier producible absorber materials. Organic solar cells show these advances. They consist of a mixture of two organic semiconducters, one donor and one acceptor material. In this work, Perylenediimide (PDI) derivatives as acceptor materials for organic solar cells were investigated and compared with each other. The synthesis of the different derivatives was completed by using perylene-3,4;9,10-tetracarboxylic acid dianhydride (PTCDA) as a starting material to achieve the 1,7-bromine derivative, which was used for the synthesis of other perylenediimide derivatives such as the 1,7-fluorine, 1,7-cyanide derivative and one consisting of two perylenemoniimide units. The yields ranged from 10 – 50%. The compounds were characterized using NMR spectroscopy, mass spectrometry, thermal analysis, as well as absorption and fluorescence spectroscopy. The optical results of the different derivatives were compared with results from density functional theory (DFT) simulations. After successful synthesis of the derivatives solar cells were assembled. The efficiencies of the assembled cells consisting PDI derivatives showed low values in the range of 0.5 to 1%.

This research gives insight into main characteristics of these materials, their potential and challenges in aspect of the synthesis and assembly of organic solar cells.

Kurzfassung

Aufgrund des steigenden Energiebedarf und der Verschmutzung verursacht durch fossile Brennstoffe, erweisen sich erneuerbare Energien als wichtigster Energieträger in der heutigen Zeit. Photovoltaikanlagen spielen hierbei eine wichtige Rolle um konventionelle Energiequellen zu ersetzen.

Solarzellen können aus verschiedensten Materialien, wie beispielsweise organische, anorganische Materialien, Polymere, sowie Hybride, hergestellt werden. Da die Herstellung von Solarzellen mit kristallinen Silizium als Absorbermaterial hohe Kosten beinhaltet, geht die Forschung immer weiter in Richtung preiswerteren und leichter herstellbaren Materialen. Diese Eigenschaften werden von organischen Solarzellen eingehalten, welche aus organischen Halbleitermaterialien (Donor und Akzeptor) bestehen. In dieser Arbeit wurden Perylenediimid (PDI)-Derivate als Akzeptormaterial für organische Solarzellen erforscht und miteinander verglichen. Die Synthese der verschiedenen Derivate wurde erreicht unter Verwendung von Perylen-3,4,9,10-tetracarbonsäuredianhydrid (PTCDA), welches als Ausgangsmaterial zur Herstellung des 1,7-bromierten Derivativs diente. Mittels diesem wurden anschließlich das 1,7-Fluor- und 1,7-Cyanidderivativ, sowie ein Derivativ bestehend aus zwei Perylenemonoimiden hergestellt. Die Ausbeuten lagen zwischen 10 und 50%. Anschließend wurden die Verbindungen mittels NMR-Spektroskopie, Massenspektrometrie, thermischer Analysen, sowie Absorption- und Fluoreszenzspektroskopie charakterisiert. Die optischen Eigenschaften wurden mit Ergebnissen aus Dichtefunktionaltheoriesimulationen (DFT) verglichen. Nach erfolgreicher Synthese der Derivative wurden diese in Solarzellen assembliert. Wirkungsgrade im Bereich von 0,5 – 1% wurden erreicht.

Diese Arbeit gibt einen Einblick in die Eigenschaften der synthetisierten Verbindungen, deren Potential, sowie den Herausforderungen im Hinblick auf Synthese und Assemblierung der organischen Solarzellen.

Acknowledgements

At this point I would like to thank those who have played a big role to the success of this work due to their professional and personal support. Especially I want to thank Prof. Gregor Trimmel for the opportunity to work on this interesting and diverse topic and the expert advice and encouragement throughout the whole thesis. Additionally, I would like to thanks Petra Kaschnitz, Josefine Hobisch, David Pfeifer and Karin Bartl for the measurements they have done for me.

My special thanks goes also to my whole working group for the friendliest working environment and the nicest coffee breaks throughout the whole thesis. Hereby, I would especially like to thanks Matiss Reinefelds for all the help in synthesis, as well as Stefan Weber and Bettina Schweda for helping me with the assembly of solar cells. Thank you again for all the useful and helpful tips you gave me.

Moreover, I would like to give a special thanks to my parents and my brother for all the support throughout my whole study and beyond and, who were always there when I needed them. Also I would like to thank all my good friends for making my life during my studies so nice and entertaining.

Table of Contents

1 Introduction

Today, the demand of energy is one of the biggest problems in mankind. Fossil fuels such as coal, oil or gas play, and will play a dominant role in global energy systems. The fundamental driver of the Industrial Revolution, as well as the technological, social, economic and development progress were fossil fuels. When it comes to fossil fuels, crude oil is the largest energy source (39%), followed by coal (33%) and natural gas (28%). The demand of this type of energy source is increasing steadily and drastically and will influence the future world immensely.
Due to their negative impacts such as local air pollution and the emitted carbon dioxide (CO_2), as well as other greenhouse gasses, the interest in renewable energies is rising from year to year.[1] In 2018 fossil fuels still dominate electricity generation. With 38% coal, 3% oil and 23% gas, fossil fuels covers 64% in total. Nuclear power shows a value of 10% and renewable energies such as hydro power, biomass and waste, wind power, solar photovoltaics and others cover around 27% with 2% electricity generation out of solar photovoltaics.[2] Since fossil fuels still cover a high percentage of the total energy production, renewable energies, such as photovoltaics, take an important part reducing conventional energy sources.

In 1839 Alexandre Edmond Becquerel had discovered the photovoltaic effect, which was back then mainly used for measuring light, since the photovoltaic power continued to be quite inefficient. In 1941 Russell Ohl invented one of the first used solar cell.[3] Since then solar photovoltaic technology is growing rapidly worldwide. The growth factor reaches a value of 57. A study in Science (2017) estimated that global photovoltaics installed capacities will be between 3 000 and 10 000 GW by 2030.[4] This would represent the needs in electricity of more than 9% of the world's population. Over 20% of all electricity could be provided by photovoltaic systems by 2050.[5]
Since the early beginnings of 1950 crystalline silicon as a material for solar cells dominated the photovoltaic market, since it is nontoxic and abundantly available in the earth's crust. Additionally they show long-term stability over decades, as well as a reduction in price of silicon modules in the last 30 years.[6] The theoretical limit for efficiency of crystalline silicon solar cells is 29.3%.[7]
Another highly researched type of solar photovoltaics are perovskite based solar cells. Due to the possibility of processing directly from solution, perovskite manufacturing is highly scalable and production costs show potential to be quite low. Additionally, they have unique properties, like their energy production capabilities, flexibilities, light weight, etc., that make them attractive for the usage in photovoltaics. However, their toxicity due to the usage of Pb^{2+} is a major disadvantage. Their efficiency increased from 3.8% in 2009[8] up to 25% in 2019 in single-junction architectures.[11]

In silicon-based tandem cells the efficiency could get even higher, up to 28%[11]. Since now perovskite solar cells have not reached sufficient operational stability to be commercialized.[9]

Way before perovskite solar cells were invented, another type of solar cells were introduced – the organic solar cells. This field of photovoltaics is a promising new technology with the potential of providing good power conversion efficiency, while being cheap, easily tunable polymeric or small molecule organic materials. An important factor is the interfacial engineering as a fundamental approach for maximizing the power conversion efficiency. In organic solar cells the light is absorbed by an active layer consisting of an electron acceptor (organic n-type material) and an electron donor (organic p-type material). Low band gap polymers and dyes are the most used donor materials. As acceptor materials fullerene derivatives, perylenediimides or other n-type materials are used.[23] Organic solar cells can reach efficiencies up to 17.4%[11].

Recently, a lot of research goes into the synthesis of non-fullerene acceptors such as perylenediimide, perylenemonoimides, as well as ITIC derivatives, which usually have a donor-acceptor-donor structure.

Therefore, the influence of different substituents in the bay-position of perylenediimide on optical and electrical properties in solar cells was investigated.

2 Theoretical Background

2.1 State of the Art

Renewable energy is one of the most important research fields since the past decades. Solar energy is one of the most important and most researched energy sources to release the world from fossil fuels. Many different kinds of solar cells were already explored. The best research-cell efficiency of the different kind of cells can be seen in Figure 1.[10]

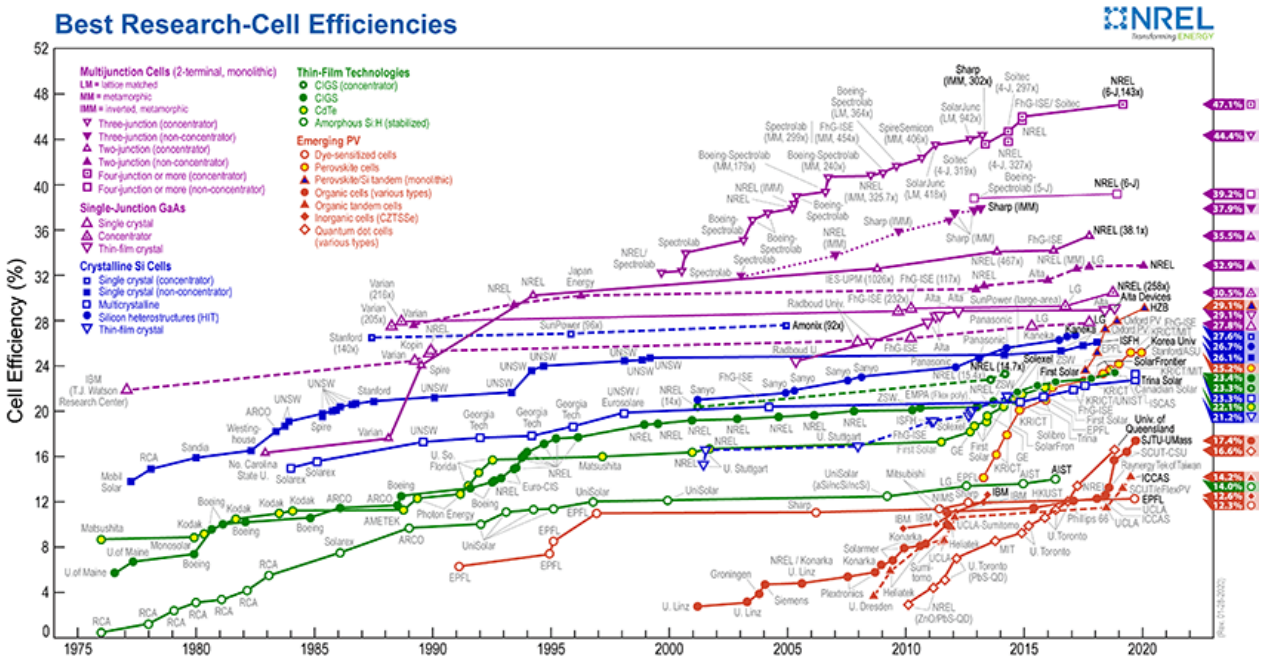

Figure 1: Best Researc-Cell Efficiencies of different types of solar cells © NREL. [11]

Most of the commercialized solar cells use inorganic materials, which provides high efficiency and has been adapted in a variety of devices, as well as in several megawatt scale plants.[12, 13] Organic solar cells still need high effort in research due to the relatively low efficiencies (Figure 1). However, organic photovoltaics show versatility of flexible thin film alternatives at relatively low costs, which make them quite attractive for further investigation. The state of the art of organic solar cells in the year 2019 already showed their potential. With efficiencies of 17.4%[11] they have been shown that they are capable to compete against other cells in the future.[12, 13]

As acceptor materials for organic solar cells fullerene derivatives were first used instead of the non-fullerenes. Over decades they showed already high power conversion efficiencies (PCE) in the field of organic photovoltaics. As an example, [6,6]-phenyl-C_{61}/C_{71}-butyric acid methyl ester ($PC_{61}BM$/$PC_{71}BM$) showed high efficiency with over 12%.[14] Due to their disadvantages like high costs, limited light absorption, etc. non-fullerene acceptors were investigated.[15] With their capability of providing strong electron-accepting properties, as well as their fully conjugated structure and their low cost, new materials were synthesized and characterized. Therefore non-fullerene acceptors were in high interest in the research field.

During the past few years, the PCE of non-fullerene based photovoltaics has increased significantly. Figure 2 shows how the interest in researching non-fullerene organic photovoltaics is rising. Year to year more publications can be observed. Therefore rising improvement in the next couple of years can be possible.[14]

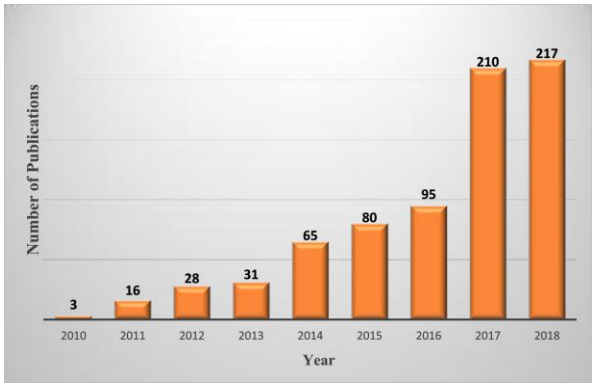

Figure 2: Number of publications in the field of non-fullerene organic solar cells[14]

Due to the increasing efficiency of organic solar cells in aspect to non-fullerene acceptors and their phenomenal characteristics, research in different perylenediimide derivatives is in high interest for the future.

2.2 Organic Solar Cells

Due to different key advantages, such as the possibility of processing directly from solution, cheap production costs and their device flexibility, photo- and electro-active organic materials are quite promising for the usage in organic photovoltaics. These organic solar cells are still under development but are receiving a lot of attention and a variety of excellent solar cells have been reported.[16] Even though several other photovoltaic technologies show higher efficiencies, organic photovoltaics (OPVs) still remain advantageous, since they have low material toxicity, costs and environmental impact. Nevertheless they exceeded certified efficiencies of 17.4%[11] to date.[17, 18]

In general a photovoltaic cell converts light into direct current electricity. Which type of light (low energy, infrared, high energy, ultraviolet photons, etc.) can be converted into electricity depends strongly on the band gap of the light-absorbing material. Therefore, a common characteristic in photovoltaics is, that a large conjugated systems of both, the small molecules and polymers, is needed. The resulting delocalized π orbital is the highest occupied molecular orbital (HOMO), which represents the valence band. The π^* orbital is the lowest unoccupied molecular orbital (LUMO) which corresponds the conduction band.[19]

2.2.1 Working Principle

The photocurrent generation in organic solar cells is based on the steps, which can be seen in Figure 3. To excite an electron from the highest occupied molecular orbital (HOMO) to the lowest unoccupied molecular orbital (LUMO), a molecule needs to absorb light. Excitation can take place in the donor, as well as acceptor material. In organic materials, different to inorganic ones, a tightly bound electron-hole pair (exciton) is formed, which has a relatively high binding energy of about 0.3 up to 1 eV.[20] For the conversion of solar energy into electric energy the excitons needs to overcome the binding energy and dissociate into electrons and holes. The dissociation can be observed at the junction, where p-type as well as n-type semiconductors are in contact and forming a D/A-interface. After the dissociation at the interface the separated charge carriers are transferred to the respective electrodes.[21, 22]

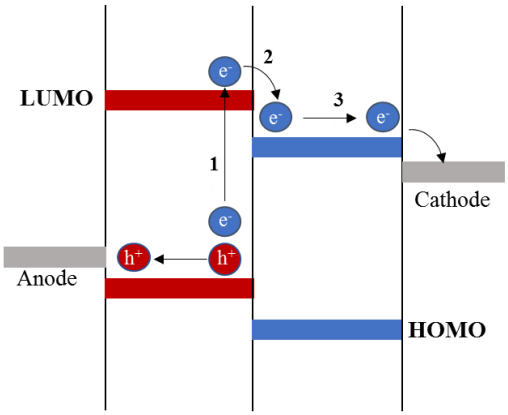

Figure 3: Working principle of an organic solar cell. 1: absorption of photon followed by excitons formation; 2: charge seperations; 3: charge extraction[23]. Graphic created by Sanela Alibegic

Efficiency of the diffusion process is depending on the excitons diffusion length (L_D), as well as the thickness of the film D_τ.

$$L_D = (D_\tau)^{\frac{1}{2}}$$

However, the excitons diffusion length limits the absorbing layer thickness. In thicker layers, the efficient conversion of sunlight into electricity is decreased, since the excitons, generated at a distance from the D/A-interface larger than $L_{D,}$ will decay to ground state before dissociating.[23]

2.2.2 Production of solar cells

For organic solar cells there are two major concepts; bilayer and bulk heterojunction. Other junction types are single layer, discrete heterojunction, graded heterojunction, as well as continuous junction.

Bilayer cells consist of two layers, which exist in between the conductive electrodes (Figure 4). Electrostatic forces are generated at the interface of the two layers due to different electron affinity and ionization energies. The materials need to be chosen wisely to make the differences large enough so that the local electric fields are strong. Another name for this junction type would be planar donor-acceptor heterojunction.
The issue of the bilayer junction type is connected with the layer thickness. The diffusion length of excitons is typically in the order of 10 nm. The diffusion for most excitons to the interface should be in the same range as the diffusion length. However, the polymer layer usually has a thickness

of at least 100 nm, which is needed to absorb enough light. This means that only a small fraction of excitons can reach the heterojunction interface because of the large thickness.[24, 25, 26, 27]

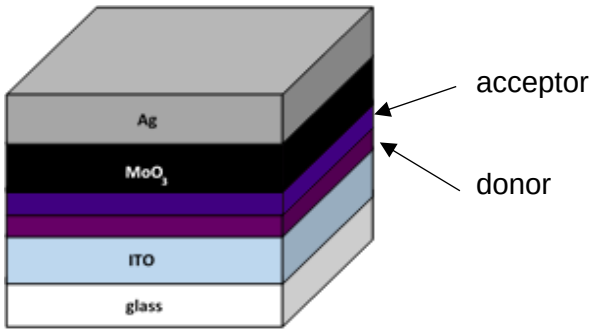

Figure 4: Bilayer Heterojunction with the active layer in the middle with the acceptor in purple and the donor in pink

Bulk heterojunction has an absorption layer consisting of a blend of donor and acceptor materials. This blend uses a domain size in the order of nanometers to allow excitons with short lifetimes to reach an interface. Dissociation takes place due to the large donor-acceptor interfacial area.[28] Bulk heterojunction has an important advantage over layered junction types, since a larger interface between donor and acceptor can be achieved. Efficient bulk heterojunctions are dependent on the large enough domain size to form a percolating network. Without this network charges can get trapped in a donor or acceptor rich domain and undergo recombination.

To achieve this junction type, a solution containing the two components is made, followed by spin coating and allowing the two phases to separate. Separation usually takes the assistance of an annealing step.[29] However, if the dispersion of the two materials is too fine, poor charge transfer through the layer can be observed.[30] The nanostructural morphology is difficult to control and therefore still critical for photovoltaic performance.[24, 24]

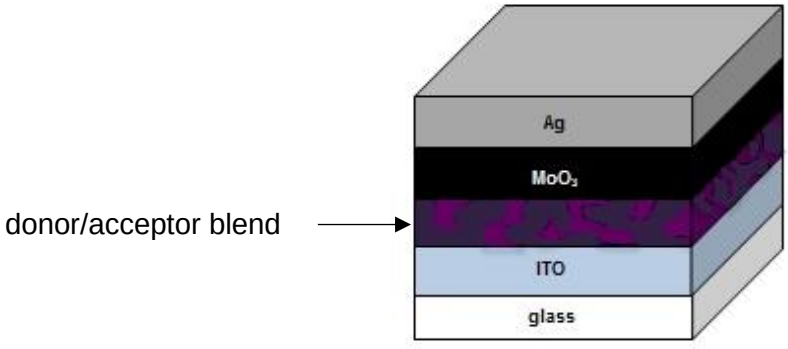

Figure 5: Bulk Heterojunction with the active layer in the middle with the acceptor in purple and the donor in pink

2.2.3 Interfacial Layer Materials

Important interfacial layer materials include inorganic metal oxides, carbon-based materials, polymers/small-molecules, metal salts/complexes, as well as organic-inorganic hybrids/composites, which have a direct impact on the efficiency and stability of the device.[31]

2.2.3.1 Electron-Transporting Materials as Cathode Interface Layers

Cathode Interface Layers (CILs) need to be highly transparent for light transmittance and stable to prevent diffusion of metal electrodes. Therefore, a lot of different materials can be used as CILs such as polymers, low working function metals, metal salts/complexes, metal oxides and so on. [31]

The most used materials among electron-transporters are n-type metal oxides with deep-lying energy levels such as ZnO[32], TiO_x[33], Nb_2O_5[34], SnO_x[35]. Organic solar cells, which are based on metal oxide CILs, show high performance due to the fact that these have outstanding features of ambient stability, high optical transparency, excellent capability to extract or transport electron carriers and good solution processability. One of the most used CIL is ZnO due to its characteristics such as low costs, non-toxicity, high stability, easy synthesis, as well as unique optical and electronic properties.[36] These materials show low working function. They match with LUMO-levels of a variety of acceptors, such as, for example, fullerenes. With variations of the crystalline structures, film morphologies, compositions and film thickness ZnO CILs can be tuned in aspect of the mobility, interfacial properties and optical transparency.[32, 32]

Similar like zinc oxide, titanium oxide is also a widely used material for CILs due to its good optical transparency, high environmental stability and relatively high electron mobility. Via spin coating, TiO_x can be fabricated as effective interfacial layers for organic solar cells. It can be used as an optical spacer to enhance light absorption and act as an electron-transporting or hole-blocking layer.

Problem with this type of metal oxide is the existence of many defects and trap sites within the layers, which gives a rise to a Schottky barrier at high working function metal/metal oxide interface or energy level mismatching at the metal oxide/bulk heterojunction layer interface. Thus, the effectiveness of titanium oxides as CILs is reduced. Light soaking with UV radiation could reduce this type of effects.[32, 33]

Another promising wide-bandgap metal oxide is tin oxide, which comes in the form of SnO_2 or SnO_x. The difference to other n-type oxides is its higher intrinsic mobility, which offers efficient carrier transport. Tin oxide CILs are very stable even upon heat treatment in comparison to other

metal oxides. Due to the small particle size, smooth film morphology and excellent electron-transporting properties of nanocrystalline SnO_2, high quality polymer/fullerene active layers were already achieved.[32, 35]

Often used as interface materials for improving solar cell performance instead of metal oxide are polymers and small-molecules, since thermal annealing of interlayers can be avoided. Also their compatibility is a huge aspect. Modification towards suitable energy levels and optical and electronic properties can be achieved easily. Due to the ability to form very thin layers and of their intermolecular dipole moments, these type of CIL materials can induce an interface dipole from the cathode to the active layer, thus reducing the working function of cathodes and increasing the built-in potential of organic solar cells.[37] Examples for organic CILs are shown in Figure 6.

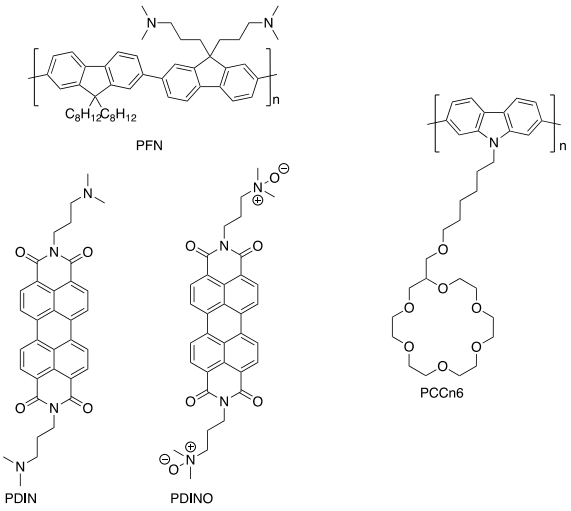

Figure 6: Molecular structures of organic CILs

Other CILs include low work function metals, metal salts/complexes and inorganic-organic hybrids and composites. [32]

2.2.3.2 Hole-Transporting Materials as Anode Interfacial Layers

In comparison with the electron-transporting cathode interface layers, the hole-transporting materials as anode interfacial layers (AIL) should have high working function to match the HOMO levels of the donor materials in the active layer to permit hole-extraction. The holes need to be efficiently transported to reduce series resistances of organic solar cells for good photovoltaic

performance. As AIL materials organic conductive polymers, graphene oxides, inorganic metal oxides/sulfides and other alternatives have been designed. [32]

PEDOT:PSS is the most used conducting polymer in AILs so far. This material offers easy solution-processing and high conductivity. Additionally, its working function matches quite well with many different polymer donors to form a good interface.[38] Problem with this conductive Polymer is the acidic and moisture sensitive characteristic, which influences the stability of the device. Modifications can help to reduce the negative aspects. [32]

In recent years, metal oxides replaced PEDOT:PSS as AILs in organic solar cells.[39] The most important material is the transition metal oxide MoO_3, due to its good transparency, better environmental stability and high working function when compared to PEDOT:PSS.[31]
Due to the higher costs of PEDOT:PSS, research tried to focus on solution-processed MoO_x-layers[40, 41, 42], which also showed better photovoltaic properties and a longer compared lifetime.[43]
Also the oxygen vacancy of the transition metal is important when taking a look at the electronic property, as well as the oxygen level, which both can be controlled by it.[41]
Another metal oxide, which can be used, is vanadium oxide (VO_x) and nickel oxide (NiO_x). Organic solar cells, which uses VO_x-AILs showed good device performance. NiO_x has a high working function, which promotes the Ohmic contact at the interface between bulk heterojunction and the anode, and acts very effective when it comes to blocking electrons.[32] Other transition metal oxides, which are suitable for AILs in organic solar cells, are WO_x[44], Fe_3O_4[45], CuO[46], RuO_2[47] and CrO_x[48].

Other promising materials which can be used as AILs for oganic solar cells can be graphene oxides and its derivatives, as well as conjugated polyelectrolytes or small-molecules as surface modifiers.[32]

2.2.4 Electrode Materials

As an electrode material transparent contacting elements are needed. Most commonly used is ITO. As Alternative PEDOT:PSS, ZnO:Al and other materials can be used.[49]

The standard transparent contact material on the substrate is indium tin oxide (ITO). It is the most used material when it comes to electrode materials.However, in the past decade the price of indium increased rapidly. Therefore, ITO may be substituted with other alternatives in the next decade. But since the main advantage of organic solar cells is their low price point, the high costs

of ITO may be outbalanced. More negative aspects of ITO are possible diffusion of indium into organic materials and its brittleness. Nevertheless solar cells with ITO as electrode materials have the potential to provide ultra-lightweight, flexible cells with a wide range of applications.[49, 50]

An alternative to indium tin oxide as electrode material can be aluminium-doped zinc oxide (ZnO:Al or often called AZO), another transparent conductive oxide (TCO). It was shown by Schulze et al. that ZnO:Al can be used as a hole contact which shows similar performance as ITO. In comparison with indium tin oxide it has similar conductivity. Problem hereby is that ZnO is chemically instable to acid, tends to grow with rough surfaces, is quite brittle and could be harmful to organic materials if deposited on top.[49, 51]

Poly(ethylene dioxythiophene):polystyrene sulfonate, short PEDOT:PSS (Figure 7), is a conductive polymer as mentioned in before. Many different formulations of PEDOT have been researched in the last couple of years. The usage of this conductive polymer ranges from antistatic coating to matrix for carbon nanotube networks as well as hole transport between ITO and organic materials.[52] Research showed that PEDOT:PSS can also be used as electrode material for polymer-based solar cells when combined with a silver grid. Additionally, PEDOT:PSS is also used as a back electrode.[53]

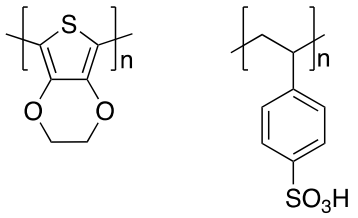

Figure 7: Structure of Poly(ethylene dioxythiophene):polystyrene sulfonate (PEDOT:PSS)

The susceptibility to oxygen, water, sodium (from glass substrates) and UV-light is a main concern when using PEDOT:PSS. Due to its conductivity of 500 S/cm it is still not comparable with ITO.[49]

Other available electrode materials would be SnO_2, Cd_2SnO_4, $CdSnO_3$, $CdInO_4$, Zn_2SnO_4, $MgIn_2O_4$, $CdSb_2O_6$ and $In_4Sn_3O_{12}$. Many of these are still under research or are not commonly used, due to toxicity of the metals such as cadmium.[49]

As back electrode, as already mentioned, PEDOT:PSS can be used. Other materials which are used as a back electrodes are, for example, Ag, Au, Al and other metals.[31]

2.2.5 Active Layer Materials

The active layer of an organic solar cell consists of a donor and acceptor material. Acceptor materials can be divided into fullerene and non-fullerene compounds. As Donors, conjugated materials are used to enable charge transport.

2.2.5.1 Donor Materials

Over the past decade the development of new donor materials had shown more interest than for acceptor materials. There has been a long history of research, which started with small molecule donors. Small donor materials, however, exhibited difficulties in forming uniform thin films from solution. To produce better organic cells, the development of new donor materials was highly necessary.[54]

An ideal polymer, which is used as a donor in organic solar cells possess various properties, such as a medium or low band gap, high carrier's mobility, matched energy levels as well as good solubility. In organic photovoltaics polymers as donor materials are used as active layers to influence the light harvesting efficiency and, as well, the device performance. Therefore it is necessary to design the polymer donor with a narrow bandgap and appropriate energy level. Examples of polymers with these characteristics are shown in Figure 8.[55]

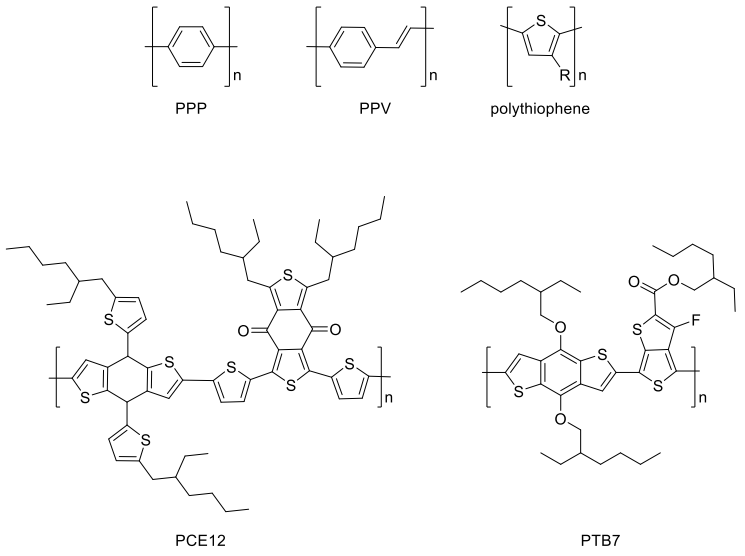

Figure 8: Donor materials for organic solar cells

2.2.5.2 Acceptor Materials

As acceptor materials hydrocarbon materials such as fullerene and non-fullerene derivatives are commonly used in the active layer of organic solar cells.

Fullerene derivatives, such as C_{60} or $PC_{60}BM$ (Figure 9), as an example, own a unique carbon structure. They are arranged in 20 hexagonal and 12 pentagonal rings with icosahedral geometry. Due to the high symmetry of these types of molecules the optical and electronic properties are favorable for the use in organic photovoltaics.[56]

Therefore they have small reorganization energy as well as the capability of accepting up to six electrons.[57] The solubility for C_{60}, however, is quite poor and could be a disadvantage when it comes to solution-processed solar cells.[58] Therefore, derivatives are already researched, such as $PC_{60}BM$[59], bis-PC_{60}[60] and so on. For enhancing the performance of the device, modifications can be used to tune the electron affinity of the fullerenes. Another possibility is the C_{70}-derivatives, which display an enhanced absorption in the visible range. Due to the lower symmetry of the fullerene cage, these derivatives additionally show an increase in the external quantum yield of the solar cell.[61]

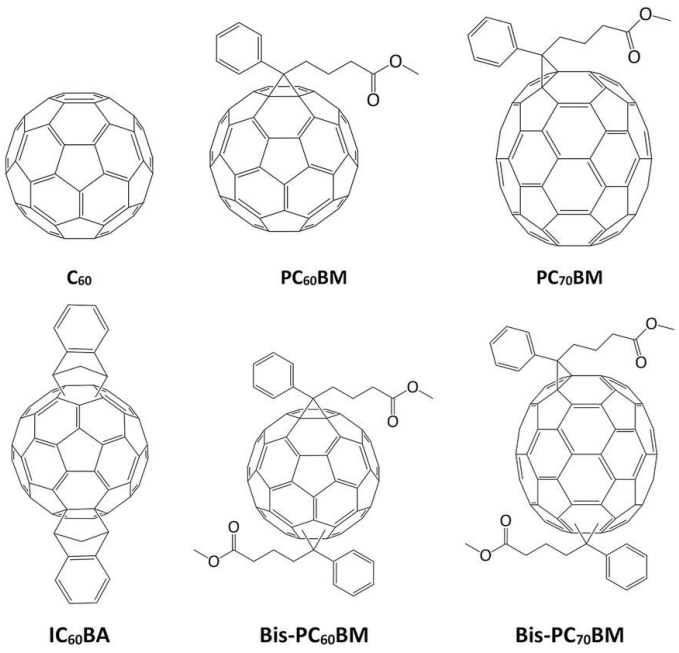

Figure 9: Fullerene acceptors for organic solar cells[61]

Fullerene acceptor materials, however, show a limited tunability of their electron affinities, thermal and photochemical instability, weak absorption in the visible and NIR regions, as well as high electron affinities and low-lying singlet excited states.[62] Additionally, the need for time-consuming purification is a high disadvantage due to the high costs involved (especially for C_{70} derivatives).
Due to the less desirable qualities of this type of active layer materials, non-fullerene acceptors such as PDI, PMI and ITIC (Figure 10) are currently a major focus of research for bulk-heterojunction organic solar cells. In comparison with fullerenes, NFAs show a wide range of variety when it comes to chemical structures and electron affinities. Additionally, they are easier synthesized. However, 2D planar conjugated organic building blocks tend to obtain inherently anisotropy crystal structures and electron transport. Therefore the formation of effective electron-extraction pathway is hindered.
Over all to say, NFAs, can exhibit strong absorptions in the region of visible and NIR spectrum, have suitably matched energy levels for charge separation with donors, the ability to form percolation pathways for charge transport, obtain the ability to form the desired morphologies for charge separation and show good molecular and morphological thermal stability and photostability.[63]

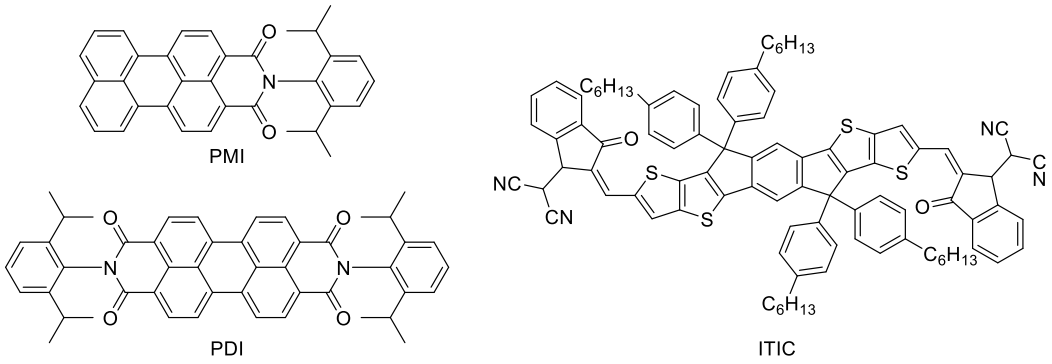

Figure 10: Non-Fullerene acceptors (NFAs) for organic solar cells

2.3 Perylene

Fullerene derivatives have been widely used as an electron acceptor in organic bulk heterojunction (BHJ) solar cells. However, these acceptors are facing some drawbacks such as the difficulty of electronic structure tuning and the high commercial value for large-scale application.[64] Due to their high chemical, thermal and photochemical stability, perylene derivatives are growing in interest as

an alternative to fullerenes. Additionally, their ability to exhibit large optical absorption in the visible to NIR spectral region is preferable. [65, 66] The most common perylene derivatives are perylene monoimides (PMI), as well as perylene diimides (PDI).

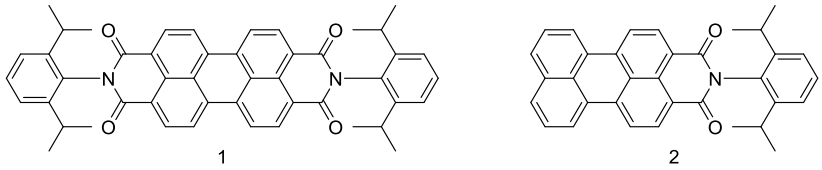

Figure 11: PDI (1) and PMI (2)

2.3.1 Perylene Diimide (PDI)

Perylene diimides (PDI) are widely used and are receiving more and more attention due to their positive characteristics such as high fluorescence quantum yield, large molar absorption coefficient, high chemical stabilities, as well as high photo and thermal stabilities under visible light irradiation.[67]

The first invention of PDI derivatives was Pigment Red (1913), were it was introduced as industrial pigment. Later on, other pigments (Pigment Red 149, Pigment Red 178; Figure 12) were developed. Due to their ability to exhibit excellent chemical, thermal, photo as well as weather stability, these types of pigments were highly used in industry. Today, they are mainly used in high-grade industrial paints, fiber applications and automobile industry. The high quality of the PDI-based pigment, as well as the durability of the colors outweighs the relatively high costs. [68]

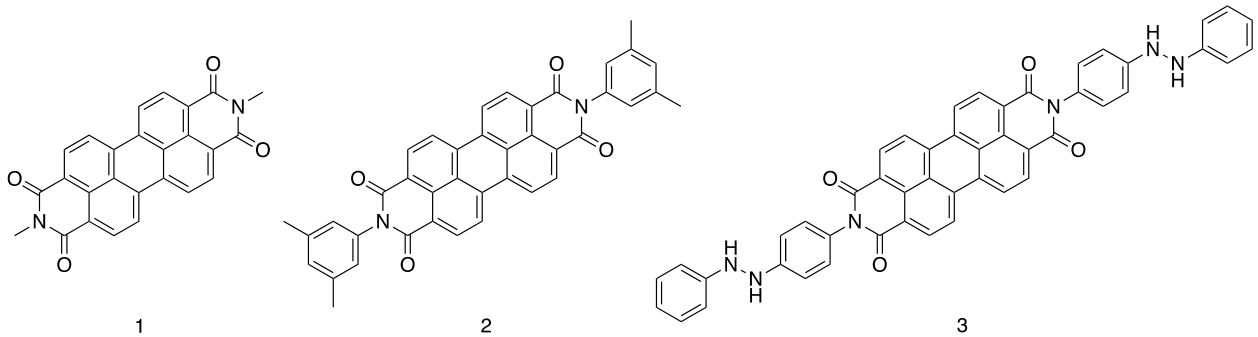

Figure 12: Pigment Red 179 (1), Pigment Red 149 (2) and Pigment Red 178 (3)

Because of their positive characteristics PDI and their derivatives developed high interest in other industrial applications. Chemical and physical properties can varied by changing the substitution pattern of the PDI. In Figure 13 the different positions, where modification can take place, are shown. Due to the symmetry elements of perylene there are three different positions available.

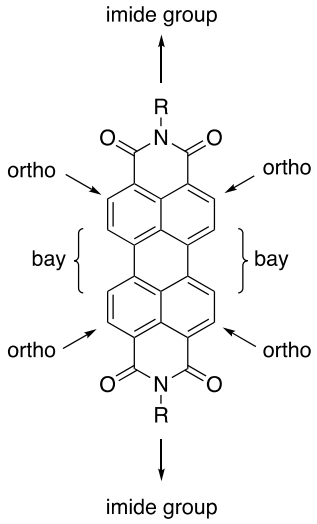

Figure 13: ortho- and bay-positions for PDI

By exchanging only the imide group of the PDI products can be achieved, which can be used for pigments as seen in Figure 12. Additionally, functional groups can be placed in the imide structure as well as the bay-position to introduce polar carboxylic acid and sulfonic acid groups. Therefore perylenes get more soluble and can be used for protein tagging.

Due to the strong electron affinities of PDI they can be used as n-channel field-effect transistors as well. For this application highly packed PDI-derivatives with electron withdrawing groups are used due to their high air stability.

Exchanging the substituents at the bay-position is researched for application such as solar cells due to the easily tunable HOMO/LUMO levels of the perylene diimide derivatives. These PDI-derivatives can reach high electron affinity, as well as high electron mobilities and therefore, they are widely used as acceptor materials. Because of the wide range of different substituents, a high amount of different derivatives are already known.[68, 69] When applied in solar cells, high power conversion efficiencies of more than 6% were already achieved (Table 1). In the following table different perylenediimide derivatives are listed.

Table 1: Perylene diimide derivatives with high efficiencies used in organic photovoltaics

Acceptor	Donor	PCE [%]
SF-PDI$_2$[70]	PffBT4T	6.30
PDI-V[71]	PtB7-Th	7.49
PM-PDI$_3$[72]	PDBT-T1	7.58
VDP-Se[73]	PBDB-T	6.01
NDP-Se[73]	PBDB-T	7.41
NP-diPDI-Se[74]	PBDB-T	6.25
BPT-Se1[75]	PDBT-T1	9.54
BPT-Se[75]	PDBT-T1	7.78
PPDI-Se[76]	PDBT-T1	7.47

In (Figure 14) the different acceptor materials from Table 1 are shown. Very high power conversion efficiencies were achieved with substituents consisting of selenium. To achieve high power conversion efficiency, when applied in photovoltaics, a complex structure is necessary, which can be seen in Figure 14. Therefore, these derivatives had more than one PDI unit to achieve PCEs over 6%. The derivatives are connected with different types of linkers. The highest PCE was achieved with BPT-Se1 and reached 9.54%. This derivative consists of four PDI units with one selenium substituent on the bay positions connected with a linker.

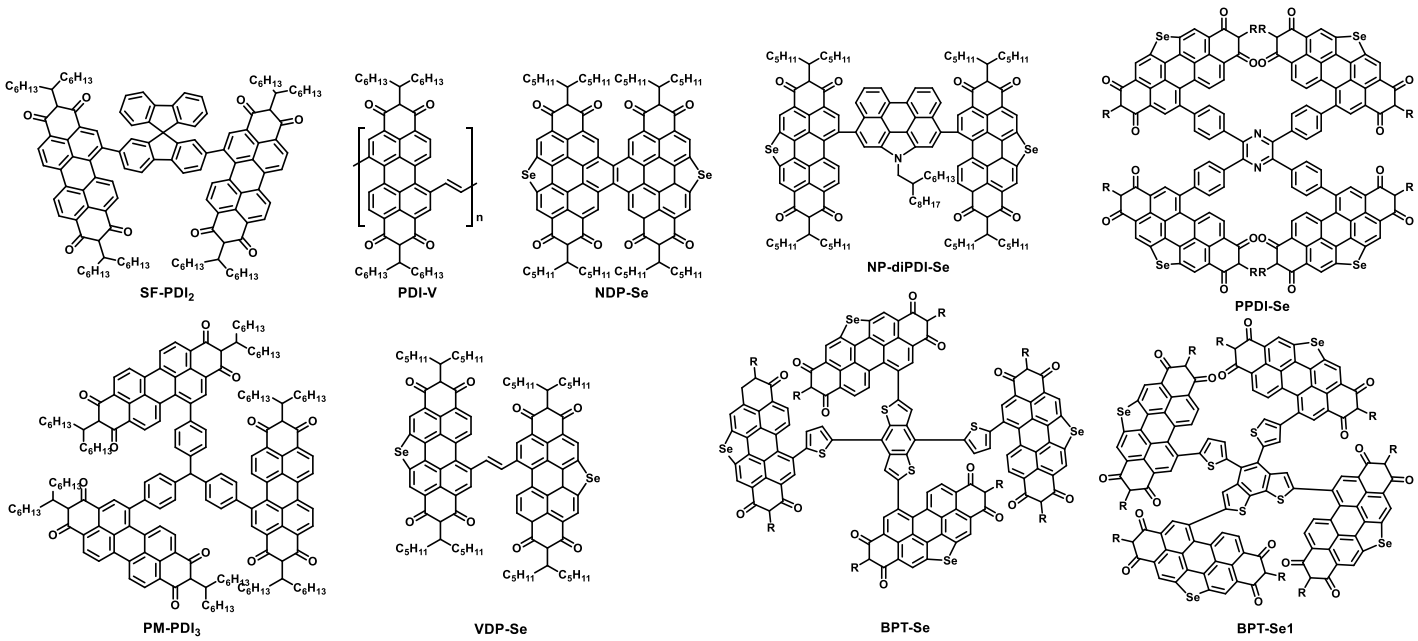

Figure 14: Perylene diimide derivatives with high efficiencies used in organic photovoltaics

2.3.2 Perylene Monoimide (PMI)

Out of all perylene based dyes the perylene monoimides (PMIs) have a higher number of available positions for chemical functionalization. The positions differ between ortho, bay and peri. These acceptors show the same positive characteristics as the PDIs such as outstanding chemical, thermal and photochemical stability. Important for PMIs is their ability to tune their strong optical absorptions from visible to NIR regions by modification. PMIs show a high number of various industrial applications such as in organic photovoltaics, optical sensors, optical memory devices, dye lasers and much more.

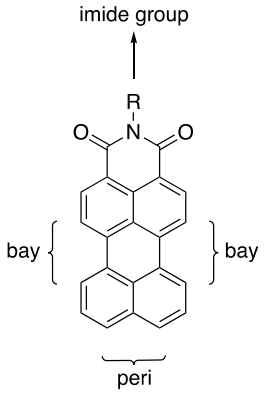

Figure 15: bay- and peri-positions of PMI

A great impact on the photo-physical properties due to energetic optical transition can be observed due to the extension of π-conjugation along peri-positions. However, the optical properties can be fine-tuned by the extension of the π-conjugation along bay-positions. π-conjugation along both peri- and bay-position is still under research due to the limited access to the key building block.[77]

3 Objective

The use of perylene diimide (PDI) derivatives as acceptors in organic solar cells should be investigated. Based on Density Functional Theory (DFT) computations by Rene Nauschnig different 1,7-substituents for this work were chosen. In the following table different acceptor materials based on PDI are shown.

Table 2: Electronic properties of different PDI derivatives (done by Rene Nauschnig)

Substance	$HOMO^{DFT}$ [eV]	$LUMO^{DFT}$ [eV]	E_G^{DFT} [eV]	λ_{max}^{DFT} [nm]	Dipole $Moment^{DFT}$ (Debye)
PDI	−6.01	−3.48	2.51	531	0.00
PDI-F_2	−6.08	−3.52	2.56	508	0.09
PDI-Cl_2	−6.19	−3.62	2.57	535	0.62
PDI- Br_2	−6.16	−3.61	2.55	541	0.45
PDI-I_2	−6.24	−3.69	2.55	532	0.19
PDI-$(CN)_2$	−6.52	−4.06	2.46	535	1.75
PDI-$(SCN)_2$	−6.46	−3.96	2.50	540	3.15
PDI-$(MeO)_2$	−5.52	−3.17	2.35	566	0.97

The main focus on this work was on halogens, as well as pseudohalogens. Since the 1,7-fluorine and 1,7-bromine showed similar electronic properties, these two were compared in organic photovoltaics. The 1,7-cyanide derivative shows an interesting difference in dipole moment when compared to the bromine or fluorine derivative. Therefore, also this type of derivative is chosen as an acceptor material. In addition, PDI-$(PMI)_2$ (perylenediimide derivative with two perylenemonoimide units) was chosen as an interesting acceptor material for organic solar cells due to the molecular size, geometry and solubility.

PDI-Br_2 was used as a starting material for all other derivatives (Scheme 1). For characterization, several measurements should be carried out. Therefore 2D NMR experiments for the identification of the molecular structure, as well as fluorescence and absorption spectroscopy for determination of the optical properties should be achieved. Additionally, thermogravimetric analysis coupled with differential scanning calorimetry has to be applied to get further information of the melting point, glass transition as well as mass loss of the products. The synthesized acceptors will be assembled in photovoltaic devices under the same conditions, as well as undergo characterization of the cell

to investigate the influence of the different substituents on the bay-position. All the assembled organic solar cells will be compared with ITIC-F.

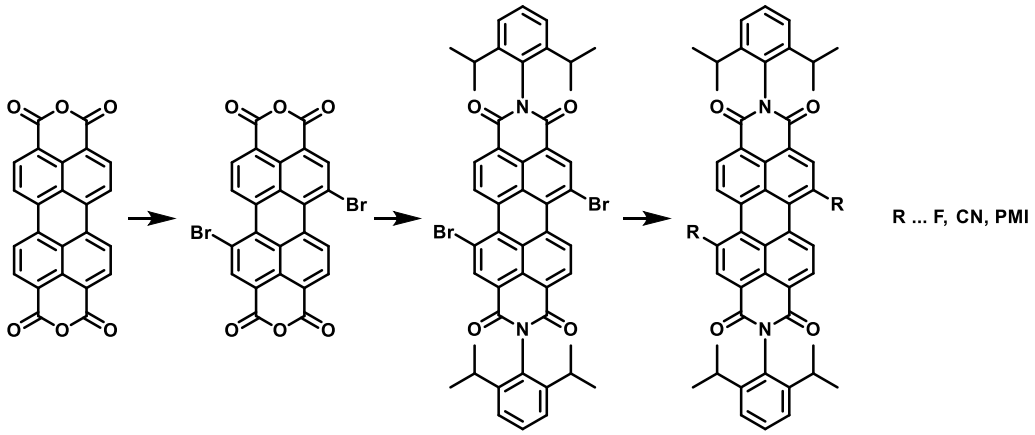

Scheme 1: Synthesis of the different PDI derivatives

4 Results and Discussion

The goal of this research was to synthesize different PDI derivatives as acceptor materials, characterize them and research their behavior in solar cells. DFT based computations were done to analyze the electronic properties of different PDI derivatives. Subsequently, the synthesis and the application in solar cells were carried out.

4.1 Synthesis of Perylene Diimide Acceptors

4.1.1 PDI-Br_2

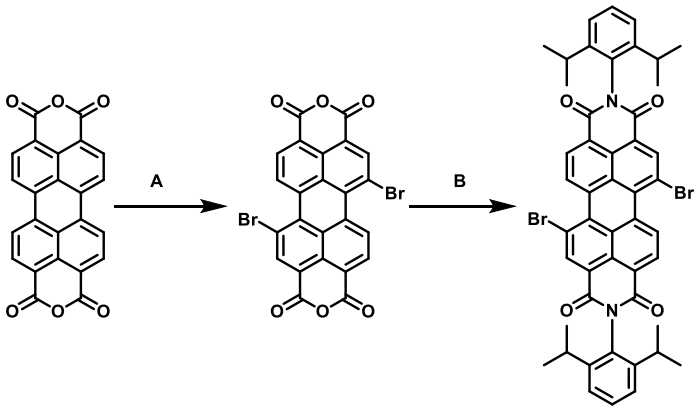

Scheme 2: Synthesis of PDI-Br_2. A: I_2, Br_2, H_2SO_4; B: 2,6-diisopropylaniline, propionic acid

The general procedure is shown in Scheme 2 and was already known in literature[67]. For the synthesis of all other derivatives, PDI-Br_2 was needed. Therefore, Perylene-3,4,9,10-tetracarboxylic dianhydride (PTCDA) was used as a starting material. In the first step, PTCDA was brominated in sulfuric acid at 80 °C using 2.2 eq. Br_2 and 0.036 eq. I_2. After 12 hours the product was immediately used for the second step. PTCDA-Br_2 reacted then with 4 eq. 2,6-diisopropylaniline in propionic acid for 48 h to PDI-Br_2. The problem with this reaction was the formation of several by-products, which were PDI-Br, PDI-Br_2, PDI-Br_3, PDI-Br_4 and others. These by-products were successfully eliminated by flash chromatography (DCM:MeOH=10:1), as well as recrystallization in DCM and MeOH. Main problem with this reaction was the formation of two different isomers (Figure 16).

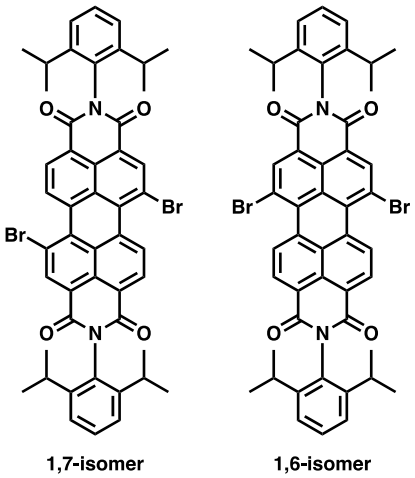

Figure 16: 1,7 - and 1,6 - isomers of PDI-Br$_2$

To isolate the 1,7-isomer several recrystallization (DCM/MeOH) steps needed to be done. NMR spectra were investigated to see, if the isomers were separated (Figure 17).

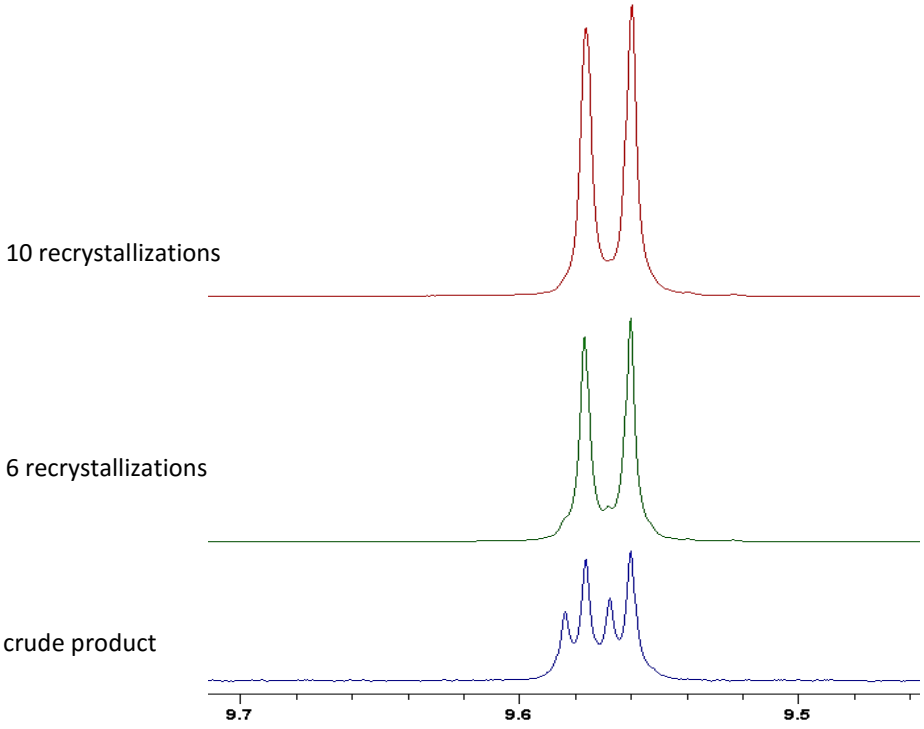

Figure 17: NMR spectra of the isolation process of the 1,7-isomer of sPDI-Br$_2$ (done by Rene Nauschnig)

As one could see in the figure above, isolation of the favored isomer took several recrystallization steps. The crude product showed 4 peaks, which are symmetric to each other, which is a sign of isomers. After six recrystallization steps the peaks were much smaller. However, both isomers where still in the mixture. Therefore, the product was recrystallized even further until the 1,7-

isomer was finally achieved (10 recrystallization steps). Due to the time consuming recrystallization steps, the isomer mixture of PDI-Br_2 was used for the first reaction of each derivative. After the successful isolation of the 1,7-PDI-Br_2 the reaction were done again and compared.

The NMR spectra in general can be seen in Figure 32 - Figure 34 (appendix). When compared with literature[67] the peaks in the spectra looked the same, which gave the conclusion, that PDI-Br_2 was successfully synthesized. However, the yield could not be determined because all three reactions were recrystallized together to get as much of the 1,7-isomer in the quickest time. Nevertheless, a yield of 70% was not achieved so far as repeated in Literature 67. The synthesized derivative was used for application in solar cells.

4.1.2 PDI-F_2

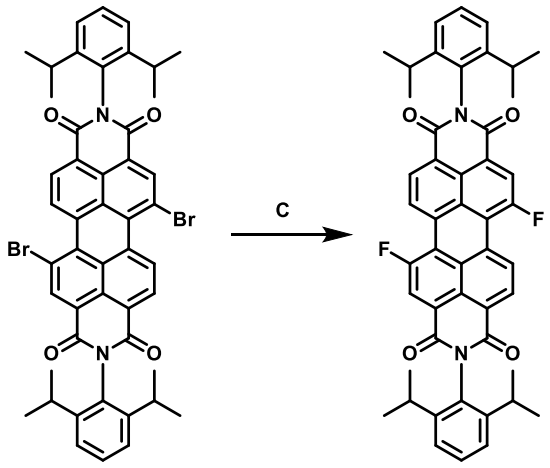

Scheme 3: Synthesis of PDI-F_2. C: KF, 18-crown-6, sulfolane

The synthesis of PDI-F_2 is depicted in Scheme 3 and was already known in literature[80]. PDI-Br_2 reacted with 6 eq. KF and 0.2 eq. 18-crown-6 at 160 °C for 1.5 h. The color turned from bright orange-red to an almost black purple. For the first reaction, whereas the isomeric mixture of PDI-Br_2 was used, a high number of by-products was found after the reaction ended, which were visible in thin layer chromatography (TLC) in DCM:MeOH (50:1). Therefore flash chromatography in the same solvent mixture was done to isolate the most prominent spot on the TLC. However, the achieved product was not PDI-F_2, which could be seen in NMR spectra (Figure 35; appendix) when compared to literature[80]. No similarities in the spectra were found. Therefore, the desired product could not be synthesized.

The second reaction was done with the isolated 1,7-isomer of the bromine derivative with the same conditions. The color turned from bright orange-red to a more orange-yellow which already was a big difference to the reaction before. TLC of the finished reaction showed only one by-product which was successfully eliminated via flash chromatography in DCM:MeOH (50:1). The isolated product was inspected with NMR spectroscopy which showed the successfully synthesized PDI-F_2 when compared with literature[80]. The peaks were comparable. Only an additional peak could be seen which showed that there was still solvent left. The spectra are depicted in Figure 36 - Figure 38 (appendix).

The synthesized derivative was used for application in solar cells.

4.1.3 PDI-$(CN)_2$

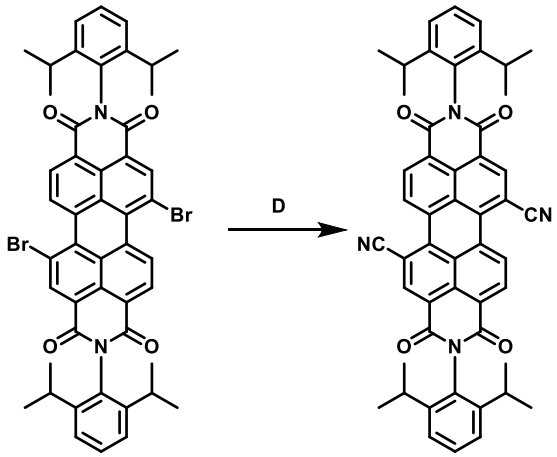

Scheme 4: Synthesis of PDI-$(CN)_2$. D: CuCN, DMF

For the synthesis of PDI-$(CN)_2$ (Scheme 4), PDI-Br_2 reacted with 20 eq. CuCN in DMF over six hours at 150 °C as seen in literature[78]. The first reaction was done with the isomeric mixture of the PDI-Br_2. Immediately the color of the mixture turned from bright orange-red to a dark purple, almost black, color. After six hours the reaction was cooled down over night. On the next day the mixture was continuously Soxhlet extracted with CH_2Cl_2 for 48 h. The solvent was evaporated. Since the product mixture was not completely soluble in DCM, it was assumed that the unsoluble particles are by-products. Therefore, filtration was performed. Afterwards, a TLC was done (CH_2Cl_2). It showed four different spots, whereas each of the spots showed a slight shadow. Therefore, flash chromatography with DCM:MeOH (100:1) was performed and the three resulting products were analyzed via NMR spectroscopy. Since neither of the three products showed the

desired PDI-$(CN)_2$ derivative in the NMR spectroscopy when compared with literature[78], a second reaction with the 1,7-isomer of PDI-Br_2 was performed.

The second reaction was carried out under the same conditions as the previous one. Only difference here was the usage of the 1,7-isomer of PDI-Br_2 as a starting material. After five minutes the reaction mixture turned from bright orange-red to a more dark red-pink color. After six hours the reaction was cooled down over night and on the next day Soxhlet extraction with CH_2Cl_2 for 24 h was performed. The solvent of the extracted mixture removed under vacuum and filtrated due to the insoluble particles. A TLC was done, which showed 2 spots. Therefore, flash chromatography with DCM was carried out and a NMR spectroscopy was performed. The spectra showed that the product was in fact the desired PDI-$(CN)_2$ derivative but there were still a few impurities which can be seen in Figure 39 - Figure 41 (appendix). Since the product had a different imide group than in literature[78], the NMR spectra from literature could only be used as reference for the aromatic region. Therefore, MS spectrometry was done (Figure 42 - Figure 44; appendix) as a prove that the desired derivative was synthesized successfully. Stilll some by-products were visible in the MS and NMR spectra. The derivative was not suitable for solar cells, since there was no time left for work-up.

4.1.4 PDI-$(PMI)_2$

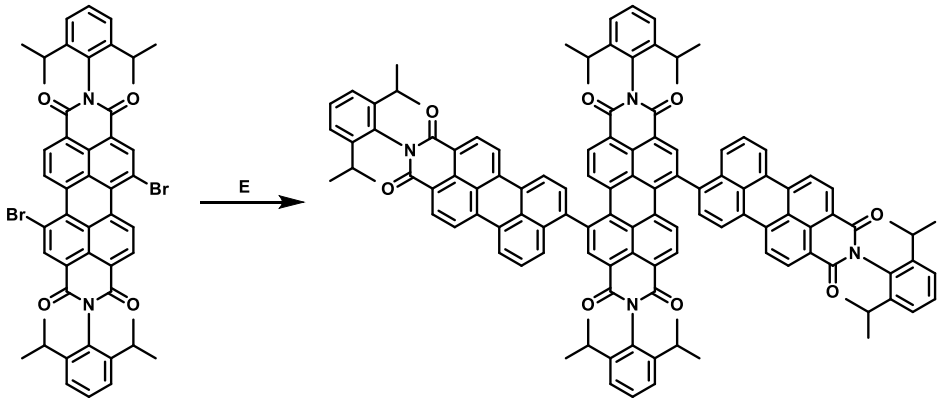

Scheme 5: Synthesis of PDI-$(PMI)_2$. E: PDI- boronic acid, pinacol ester, $Pd(PPh_3)_4$, KF, EtOH, Aliquat, toluene

For the first reaction the isomeric mixture of PDI-Br_2, for the second one, the 1,7-isomer was used for the synthesis of the $(PMI)_2$ derivative. In comparison to the reactions above there was no major difference in color or by-products of the two different reactions.

For the PDI-$(PMI)_2$ derivative a Suzuki cross coupling reaction was used[79], where PDI-Br_2, PMI-boronic acid, pinacol ester, KF, EtOH, Aliquat and a palladium catalyst reacted in toluene under N_2 atmosphere at 100 °C. After 10 min the reaction mixture turned dark red. The reaction was controlled via TLC. After 1 day the TLC showed that the reaction was not finished so another spatula of the catalyst as well as 10 mL toluene were added to the mixture. The reaction was stirred at 100°C for another day. After the reaction finished the organic phase was separated and dried with Na_2SO_4. Since the Na_2SO_4 remained in a dark red color after washing with toluene, it was assumed that product was absorbed to the powder. Therefore the remaining dark red Na_2SO_4 was washed in DCM and a TLC of the toluene as well as the DCM fraction was carried out. The fraction with DCM showed no by-products, whereas the toluene fraction showed plenty. Both fractions were dried over vacuum. A chromatography column (DCM) was done of the toluene fraction to remove the by-products. Further recrystallization of both fraction was done. NMR spectra was used to take a look at the different products after recrystallization. However, each fraction showed plenty of by-products and it was not quite sure if the resulting product was the $(PMI)_2$ derivative. Since too many by-products were visible in the NMR spectra (Figure 45 - Figure 46),it was not possible to evaluate it.

4.1.5 Optical Characteristics

Absorption spectra were recorded in $CHCl_3$ to see the optical properties of the products. The molar absorption coefficients were determined by the concentrations of the acceptor, as well as the absorption of each sample. The absorption spectra from the different PDI derivatives, as well as PDI itself, are shown in Figure 18 with normalized absorption values.

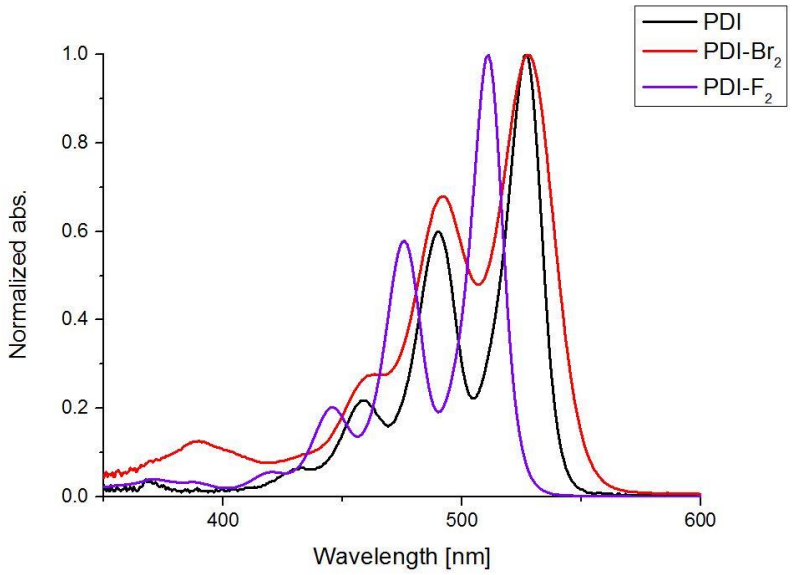

Figure 18: Absorption spectra of each acceptor dissolved in $CHCl_3$; red: PDI-Br_2m, purple: PDI-F_2, black: PDI; PMI measured by Rene Nauschnig

As one could see in Figure 18, the absorption of PDI as well as the bromine derivative was almost the same. Only a slight shift to a higher wavelength could be observed. However, the fluorine derivative showed a more visible difference when compared to PDI. A shift to smaller wavelength was noticeable.

Additionally, the molar absorption coefficient (ε) was calculated by using the formula beneath with the concentration c of the absorbing species per unit volume, the distance L that the light travels through the solution and the amount of light absorbed by the sample (A).

$$\varepsilon = \frac{A}{Lc}$$

The molar absorption coefficient for the fluorine derivative was higher in comparison with PDI-Br_2 and showed a value of 91 000 L mol^{-1} cm^{-1}. For PDI-Br_2 it reached 71 500 L mol^{-1} cm^{-1}. However, the values are still quite similar and could be described by the effect of a rather flat perylene core instead of a twisted one.

Out of the absorption spectra the band gap ($E_G^{opt.}$) was determined for both acceptor materials. A tangent was applied were the peak flattens out. The value in nanometers can be read off the x-axis and was transformed into eV. The resulting band gaps were compared with the computed data for both acceptors and were listed in Table 3.

Table 3: Optical band gaps and absorption maxima determined graphically from absorption spectra and by DFT based computations in the gas phase (6-31+G)*

Substance	E_G^{opt} [eV]	λ_{max}^{opt} [nm]	E_G^{DFT} [eV]	λ_{max}^{DFT} [nm]
PDI-F_2	2.37	510	2.56	508
PDI- Br_2	2.27	521	2.55	541

The values of the DFT based computations were achieve by experiments in gas phase (6-31+G*). The band gap for both derivatives showed smaller values by optical determination when compared with DFT computations. The absorption maxima however, showed a quite accurate value for PDI-F_2, whereas the value of PDI-Br_2 was again decreased.

Additionally, fluorescence spectra were recorded for each derivative in $CHCl_3$, as well as the relative quantum yield Φ was calculated from the obtained data. The fluorescence and absorption spectra of both derivatives are shown in Figure 19; in red: absorption spectra of PDI-Br_2, in purple: absorption spectra of PDI-F_2 and in black the emission spectra of the derivatives. The stokes shift shows quite small values for both derivatives (PDI-Br_2: 28.0 nm; PDI-F_2: 8.2 nm), which indicates rigid structure of the molecules.[80]

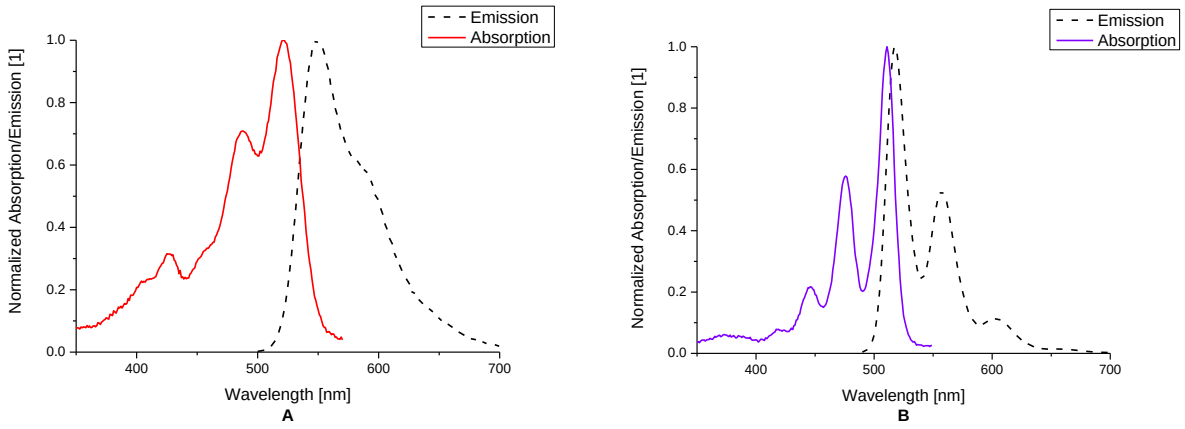

Figure 19: Absorption (red, purple line) and fluorescence spectra (black, dashed line) of both PDI derivatives in solution ($CHCl_3$); A: PDI-Br_2; B: PDI-F_2

The quantum yield was calculated out of the experimental data using “Fluoreszenzorange” as a reference material with a quantum yield of over 90%[81]. For PDI-Br_2 the yield reached 91.6 $\pm$ 0.08%, for PDI-F_2 100.0 $\pm$ 0.01%. The quantum yield showed similar values for both derivatives.

4.1.6 Thermal Characteristics

The synthesized PDI derivatives were characterized by thermogravimetric analysis (TGA) and differential scanning calorimetry (DSC). In Figure 20 the results of the TGA measurement coupled with a DSC for the PDI-Br_2 and PDI-F_2 derivative are illustrated.

Figure 20A shows the curves for PDI-F_2. No mass loss could be observed at the beginning of the analysis. The compound starts melting at 414 °C and subsequently decomposes. The mass loss, which can be observed reaches a value of 36% in total.

Figure 20B shows the curves for PDI-Br_2. As well as the fluorine derivative, PDI-Br_2 shows no visible mass loss at the beginning. No melting point was observed. However, an exothermic peak at 439 °C was visible, which indicates decomposition. After decomposition a mass loss of around 37% in total can be observed. Compared to the PDI-F_2 compound it is almost exactly the same value. Both PDI derivatives showed high thermic stability even at high temperatures.

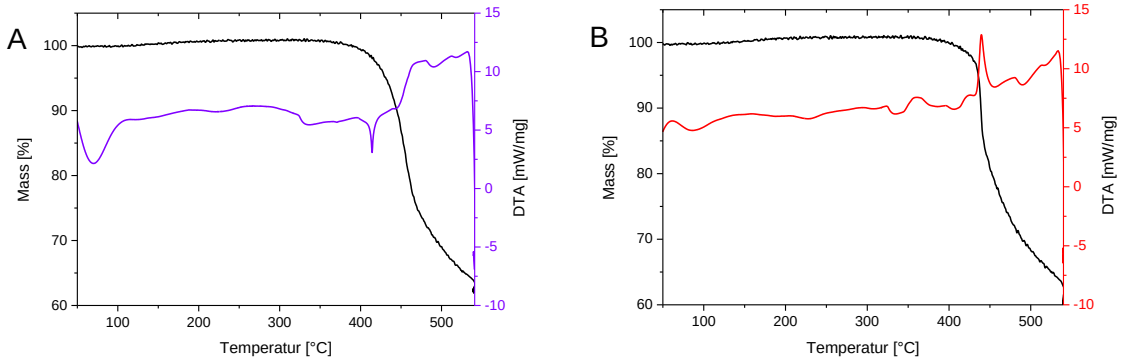

Figure 20: TGA measurement coupled with DSC for PDI-F_2 (left) and PDI-Br_2 (right)

4.2 Organic Solar Cells

The assembly of the organic solar cell devices can be seen in Figure 21. ITO-coated glass substrates were used and coated with ZnO as an electron transport layer, the active layer, which consists of acceptor and donor material, the hole transport layer (MoO_3) and the top electrode (Ag).

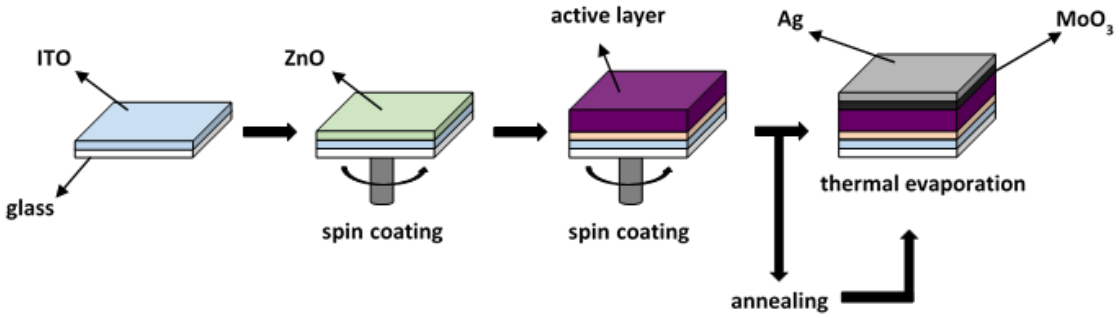

Figure 21: Assembly of organic solar cell devices

For the first experiment ITIC-F and PDI-Br_2 was used. The second experiment was done with PDI-F_2. ITIC-F was used for comparison reasons, since it has high efficiency values. For all acceptors PCE-12 as a donor material was chosen. All acceptor, as well as donor materials can be seen in Figure 21. All experiments were done with the same conditions, despite PDI-Br_2 needed different spin coating parameters, due to too thin layers.

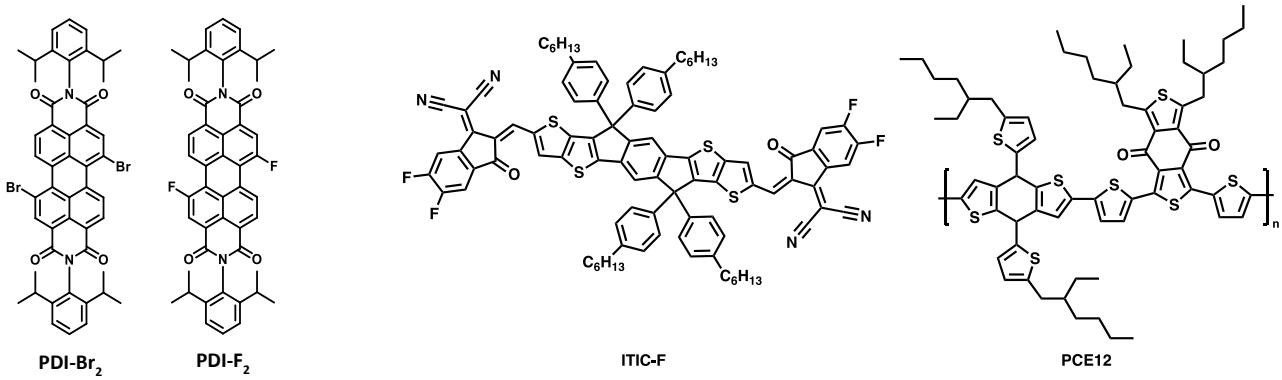

Figure 22: Acceptor (PDI-Br_2, PDI-F_2, ITIC-F) and donor (PCE12) materials for organic solar cells

4.2.1 ITIC-F

For the first experiment of organic solar cells ITIC-F was used as an acceptor material for comparison reasons with the acceptor materials, due to the fact of high power conversion efficiency values. The acceptor and donor (PCE12) were dissolved in chlorobenzene in a concentration of 10 mg/mL (results are shown in Table 4). Both materials were dissolved completely under heating of 50 °C. A donor/acceptor blend was made. The active layer consisting of donor and acceptor were spin coated with the same parameters for all substrates. Eight devices were assembled. The mean values for each annealing temperature are depicted in Table 4.

Table 4: Results of organic solar cells with ITIC-F as acceptor and PCE12 as donor material in a ratio 1:1 with a concentration of 10 mg/mL. Mean values of 12 cells.

	V_{OC} [V]	I_{SC} [mA/cm2]	FF [1]	PCE [%]	Annealing
ITIC-F PCE12 1:1 10 mg/mL	0.65 ± 0.02	-14.68 ± 0.42	0.39 ± 0.00	3.59 ± 0.20	-
	0.55 ± 0.10	-15.01 ± 0.90	0.46 ± 0.10	3.85 ± 1.10	100°C, 10 min
	0.55 ± 0.09	-14.64 ± 0.81	0.45 ± 0.09	3.60 ± 1.12	160 °C, 10 min
	0.47 ± 0.08	-16.61 ± 0.98	0.51 ± 0.10	4.10 ± 0.07	200 °C, 10 min
Best Cell	**0.49**	**-19.34**	**0.54**	**5.12**	**200 °C, 10 min**

As one could see in Table 4 the fill factor, as well as the power conversion efficiency is increasing at higher annealing temperatures. However, the open circuit voltage showed a decrease. No trend could be observed for the I_{SC}.

The highest PCE was observed at 200 °C with 5.12%. For this cell, the fill factor (FF) had a value of 54%. The open circuit voltage (V_{OC}) had a value of 0.49 V. The IV characteristics of the best assembled solar cell is depicted in Figure 23.

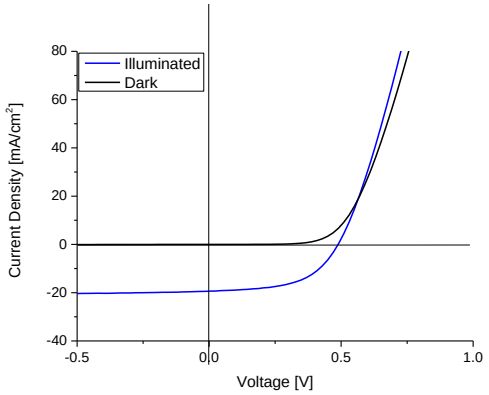

Figure 23: IV characteristics of the best solar cell with ITIC-F as acceptor and PCE12 as donor material of the dark (black) and illuminated measurement (blue).

Since the best cell was achieved at 200 °C annealing temperature, it was assumed, that higher annealing temperatures have a positive effect on this type of material. Nevertheless, only presumptions can be made, since only eight devices of ITIC-F for solar cells were made. Further optimization would be desirable.

The layer thickness and roughness of the active layer of organic solar cells were measured with a contact profilometer. The values are depicted in Table 5. Two different annealing steps were compared; one without annealing and one with an annealing temperature of 100 °C. The average of layer thickness of the active layer of both devices was 64.1 $\pm$ 16.2 nm. The roughness of both devices showed an average of 2.7 $\pm$ 1.3 nm. As depicted in Table 5, the layer thickness, as well as the roughness, showed different values at different positions on the substrate. Therefore, further optimization (spin coating parameters, donor/acceptor ratio and concentration) need to be done. Since the average values for layer thickness for both substrates showed only slight differences, one would expect similar values for the PCE. However, the power conversion efficiency showed different values, due to the high difference in layer thickness at each position. Additionally, the highest value reached 79.9 nm without annealing and 88.1nm at 100 °C annealing temperature. The lowest value was 37.1 nm without annealing and 42.2 nm at 100 °C annealing temperature. The difference in thickness could be assumed as reason for the fluctuations in PCE as well.

Table 5: Comparison of the layer thickness of the active layer of organic solar cells with ITIC-F as acceptor and PCE as donor material on 5 different positions on the substrate

no annealing		**annealed at 100 °C**	
Layer Thickness [nm]	**Roughness [nm]**	**Layer Thickness [nm]**	**Roughness [nm]**
37.1	2.8	42.2	5.6
76.7	1.1	88.1	2.2
51.6	4.4	77.8	1.8
79.9	2.7	69.9	1.2
60.6	2.7	57.4	2.2
61.2 $\pm$ 15.9	**2.7 $\pm$ 1.0**	**67.1 $\pm$ 16.0**	**2.6 $\pm$ 1.5**

Additionally images of the cells at 100 °C, 160 °C and 200 °C were recorded using a light microscope with a magnification 500x (Figure 24). The active layer in all three substrates showed a smooth and homogeneous surface without crystallites. Therefore, it can be assumed that donor

and acceptor were perfectly dissolved in the solution. However, small particles could be observed all over the different substrates, which was assumed to be dust particles.

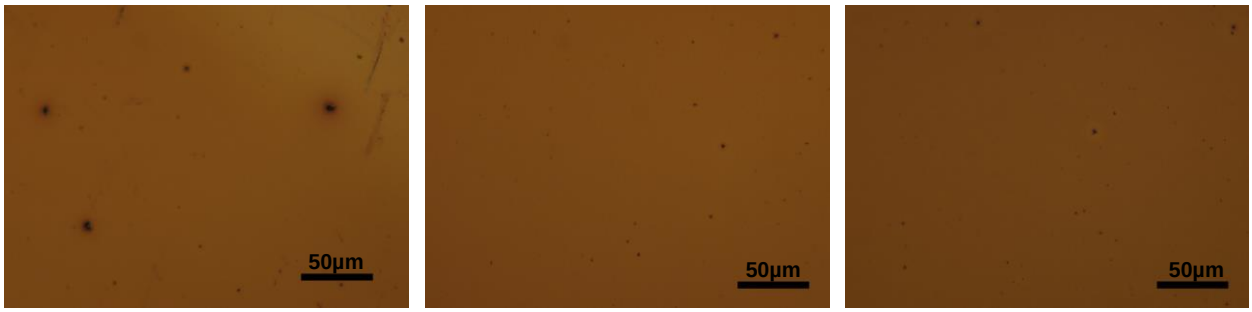

Figure 24 Images with a magnification of 500x of the active layer of organic solar cells with an annealing temperature of 100°C (left), 160 °C (middle) and 200 °C (right) containing ITIC-F and PCE12 as active layer materials.

4.2.2 PDI-Br_2

For the next experiment, PDI-Br_2 as an acceptor material was used. The acceptor, as well as the donor (PCE12) were dissolved in chlorobenzene in a concentration of 10 mg/mL. The mean values are shown in Table 6. Both materials were dissolved completely under heating of 50 °C. A donor/acceptor blend was made. The solid was immediately dissolved under heating of 50 °C. Since the layer thickness was too thin, the active layer consisting of donor and acceptor were spin coated with different spin coating parameters. Six devices were spin coated with the same optimized parameters and reached an acceptable thickness. The layer thickness of each device can be compared in Table 7.

Table 6: Results of organic solar cells with PDI-Br_2 as acceptor and PCE12 as donor material in a ratio 1:1 with a concentration of 10 mg/mL. Mean values of 6 or 12 cells

	V_{OC} [V]	I_{SC} [mA/cm2]	FF [1]	PCE [%]	Annealing
PDI-Br_2 PCE12 1:1 10 mg/mL	0.59 ± 0.00	-3.35 ± 0.12	0.34 ± 0.01	0.65 ± 0.04	-
	0.57 ± 0.00	-2.77 ± 0.14	0.35 ± 0.01	0.55 ± 0.04	-
	0.57 ± 0.00	-2.86 ± 0.27	0.34 ± 0.33	0.56 ± 0.10	-
	0.55 ± 0.01	-3.84 ± 0.24	0.33 ± 0.01	0.70 ± 0.06	160 °C, 10 min
	0.53 ± 0.00	-4.35 ± 0.21	0.31 ± 0.01	0.71 ± 0.04	200 °C, 10 min
Best Cell	**0.57**	**-3.56**	**0.4**	**0.81**	**-**

In Table 6 one could see the decrease in V_{OC} and FF with higher annealing temperatures. However, an increase was observed for the PCE, as well as I_{SC}. However, the highest PCE was achieved without annealing and had a value of 0.81%. For this cell the FF showed a value of 40%.

The V_{OC} had a value of 0.57 V. The IV characteristics of the best assembled solar cell is depicted in Figure 25.

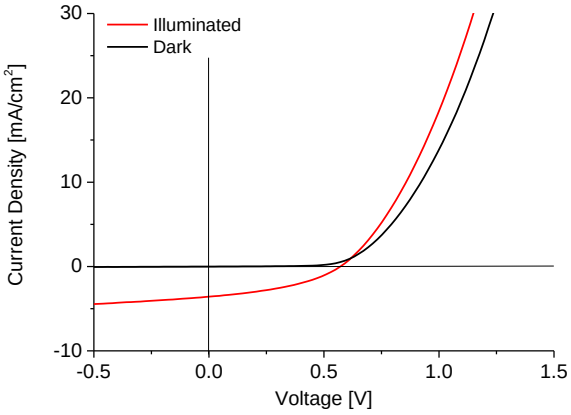

Figure 25: IV characteristics of the best solar cell with PDI-Br_2 as acceptor and PCE12 as donor material of the dark (black) and illuminated measurement (red).

Since the best cell was achieved at 160 °C annealing temperature, it was assumed, that a higher annealing temperature had a positive effect on this material. Since only eight devices were made, further optimization is needed to get an exact insight of the annealing behavior.

In Table 7 the layer thickness, as well as the roughness is depicted. Devices with no annealing temperature but different spin coating parameters were measured with a contact profilometer. The layer thickness of both devices showed different thicknesses, which was visible with the eye and therefore expected. Both of the measured devices showed variation of layer thickness on the different positions. However, the roughness stayed quite the same. Even though the layer thickness of both substrates showed different values, the PCE was similar. Therefore the layer thickness had no influence on the efficiency of solar cells with the bromine derivative as acceptor material. The average value of layer thickness of the active layers of both devices was 76.3 $\pm$ 14.5 nm with a roughness of 2.2 $\pm$ 1.4 nm.

Table 7: Layer thickness of the active layer of organic solar cells with PDI-Br_2 as acceptor and PCE as donor material on 5 different positions on the substrate

1500 rpm/no annealing		1000 rpm/no annealing	
Layer Thickness [nm]	**Roughness [nm]**	**Layer Thickness [nm]**	**Roughness [nm]**
78.5	3.2	59.1	1.4
57.6	1.3	101.0	1.3
68.9	1.2	76.5	2.2
76.8	2.0	92.0	6.0
59.9	1.9	92.8	1.5
68.3 ± 8.5	**1.9 ± 0.7**	**84.3 ± 14.9**	**2.5 ± 1.8**

Additionally images of the cells with the same spin coating parameters at different annealing temperatures (no annealing, 160 °C and 200 °C) were recorded using a light microscope with a magnification 500x (Figure 26). The active layer in all substrates showed a smooth and homogeneous surface without crystallites. Therefore, it can be assumed that donor and acceptor were perfectly dissolved in the solution. However, all over the not annealed devices dust particles were be observed.

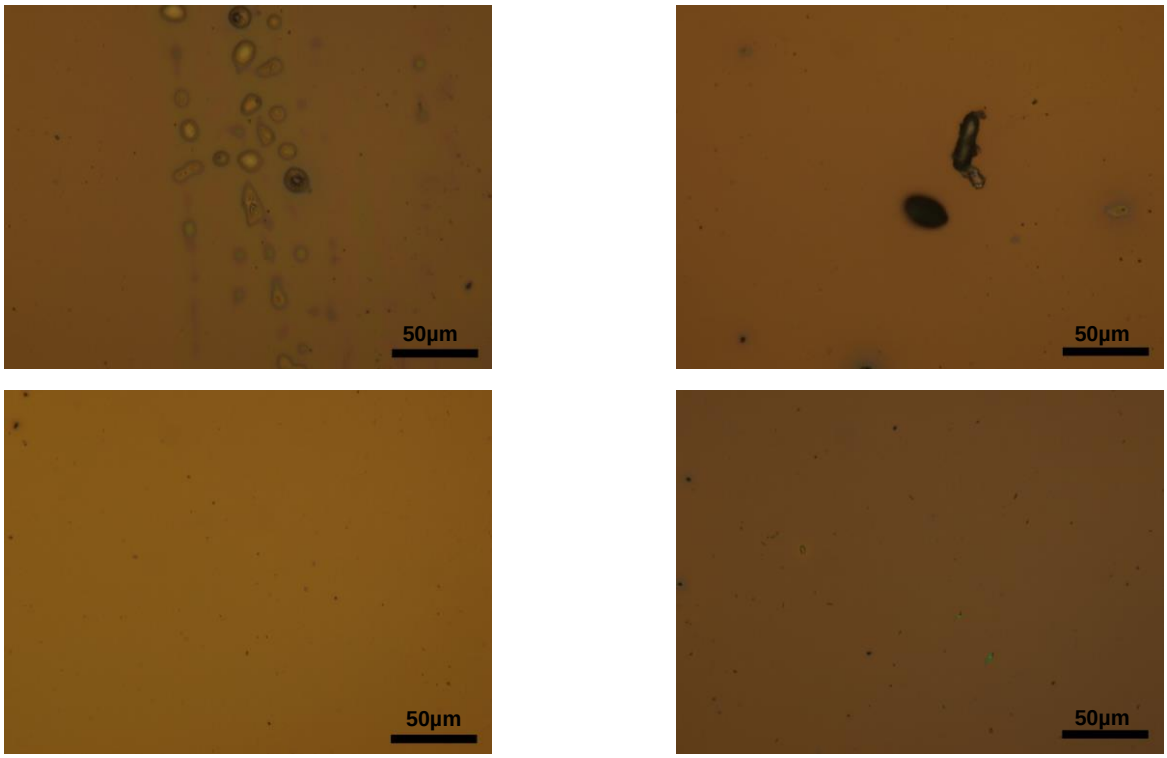

Figure 26: Images with a magnification of 500x of the active layer of organic solar cells without annealing (top left, top right), with 160 °C (bottom left) and 200 °C annealing temperature (bottom right) containing PDI-Br_2 and PCE12 as active layer materials.

4.2.3 PDI-F_2

For the last experiment, PDI-F_2 was used as an acceptor material. The acceptor and donor (PCE12) were dissolved in chlorobenzene in a concentration of 10 mg/mL. The mean values are depicted in Table 8. Both materials were dissolved completely under heating of 50 °C. A donor/acceptor blend was made. The active layer consisting of donor and acceptor were spin coated with the same parameters for all 16 devices. The annealing temperature was varied.

Table 8: Results of organic solar cells with PDI-F_2 as acceptor and PCE12 as donor material in a ratio 1:1 with a concentration of 10 mg/mL. Mean values of 6 or 12 cells

	V_{OC} [V]	**I_{SC} [mA/cm2]**	**FF [1]**	**PCE [%]**	**Annealing**
PDI-F_2 PCE12 1:1 10 mg/mL	0.70 ± 0.02	-1.56 ± 0.13	0.42 ± 0.02	0.44 ± 0.04	-
	0.67 ± 0.01	-1.73 ± 0.10	0.45 ± 0.02	0.53 ± 0.03	100 °C, 10 min
	0.67 ± 0.02	-2.52 ± 0.17	0.45 ± 0.02	0.75 ± 0.06	120 °C, 10 min
	0.66 ± 0.02	-2.01 ± 0.16	0.45 ± 0.02	0.60 ± 0.05	140 °C, 10 min
	0.63 ± 0.01	-2.16 ± 0.17	0.46 ± 0.02	0.62 ± 0.06	160 °C, 10 min
	0.69 ± 0.02	-1.91 ± 0.11	0.44 ± 0.02	0.57 ± 0.03	180 °C, 10 min
	0.57 ± 0.11	-1.96 ± 0.31	0.39 ± 0.05	0.41 ± 0.11	200 °C, 10 min
Best Cell	**0.69**	**-3.23**	**0.44**	**0.96**	**120 °C, 10 min**

With higher annealing temperature the values of the PCE increased until 140 °C and decreased for higher temperatures. The same behavior could be observed for the I_{SC}. The FF showed no influence. A decrease with higher annealing temperatures in V_{OC} was observable.

The highest PCE of 0.96% was observed at 120°C annealing. For this cell, the FF showed a value of 44%. The V_{OC} had a value of 0.63. The IV characteristics of the best assembled solar cell is depicted in Figure 27.

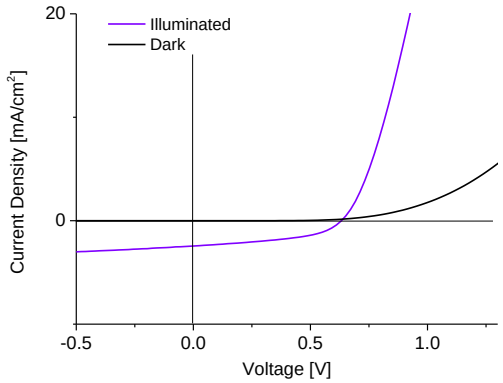

Figure 27: IV characteristics of the best solar cell with PDI-F_2 as acceptor and PCE12 as donor material of the dark (black) and illuminated measurement (purple).

Additionally, the layer thickness, as well as the roughness were measured with a contact profilometer (Table 9). Even though the spin coating parameters for all substrates stayed the same, the layer thickness and roughness showed big differences. It can be assumed that the mixture of donor and acceptor was too concentrated and therefore difficulties with spin coating occurred. However, the average layer thickness of the active layer of both devices had a value of 111.2 $\pm$ 24.4 nm and a roughness of 2.2 $\pm$ 1.0 nm.

Table 9: Layer thickness of the active of organic solar cells with PDI-Br_2 as acceptor and PCE as donor material on 5 different positions on the substrate

no annealing		**annealed at 100°C**	
Layer Thickness [nm]	**Roughness [nm]**	**Layer Thickness [nm]**	**Roughness [nm]**
112.0	3.6	80.5	1.1
173.0	4.1	87.2	0.9
98.7	2.5	119.0	1.3
114.0	1.8	105.0	2.0
124.4	2.7	97.9	2.2
124.4 $\pm$ 25.6	**2.9 $\pm$ 0.8**	**97.9 $\pm$ 13.5**	**1.5 $\pm$ 0.5**

Images of the cells at different annealing temperatures (120 °C, 140 °C, 160 °C, 200 °C) were recorded using a light microscope with a magnification 500x (Figure 28). The active layer at 120 °C and 160 °C showed that the donor/acceptor mixture wasn't dissolved properly. Therefore crystallites were visible all over the substrate. However, these substrates showed the highest PCE.

At 140 °C and 200°C annealing temperature, pores were visible due to dust particles. However, a homogeneous surface without crystallites was observed. The PCE of these substrates showed the weakest behavior.

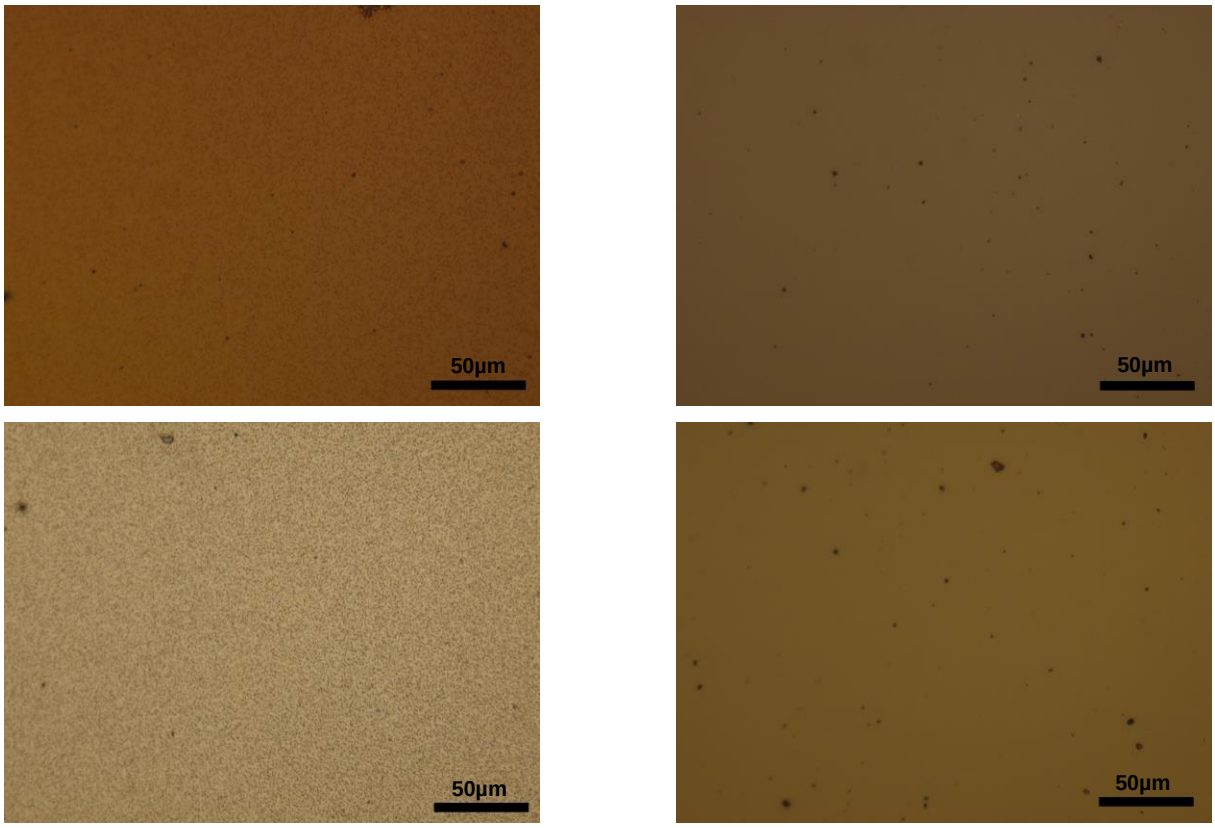

Figure 28: Images with a magnification of 500x of the active layer of organic solar cells with an annealing temperature of 120 °C (top left), 140 °C (top right), 160 °C (bottom left) and 200 °C (bottom right) containing PDI-F_2 and PCE12 as active layer materials.

4.2.4 Comparison

The performance of the cells depends highly on annealing temperature and the solubility of the donor/acceptor blend. The IV characteristics, as well as the layer thickness of one cell of each acceptors at no annealing temperature are depicted in Table 10 for further comparison.

Table 10: IV characteristics and active layer thickness of solar cells with the different acceptor materials (ITIC-F, PDI-Br_2, PDI-F_2) and PCE12 as a donor in the ratio 1:1 with a concentration of 10 mg/mL. The best cell is shown in brackets.

	V_{oc} [V]	I_{sc} [mA/cm2]	FF [1]	PCE [%]	Layer Thickness [nm]
ITIC-F	0.65 (0.49)	-13.72 (-19.34)	0.39 (0.54)	3.41 (5.12)	61.17
PDI-Br_2	0.57 (0.57)	-2.77 (-3.56)	0.35 (0.40)	0.55 (0.81)	68.31
PDI-F_2	0.68 (0.69)	-1.49 (-3.23)	0.42 (0.44)	0.42 (0.96)	124.42

Comparison of the three different acceptor materials could not be achieved properly due to their different layer thickness (PDI-Br_2 compared with PDI-F_2). ITIC-F showed a much higher PCE than the other materials, which was already expected. PDI-Br_2 showed a higher efficiency than PDI-F_2 when no annealing took place. However, the best cells showed the exact opposite effect. Therefore, both materials need to undergo further investigation to get a better feeling about annealing temperatures, layer thickness, as well as IV characteristics.

Absorption spectra were recorded for each acceptor, the donor, as well as the blend of both in films. The spectra are depicted in Figure 29.

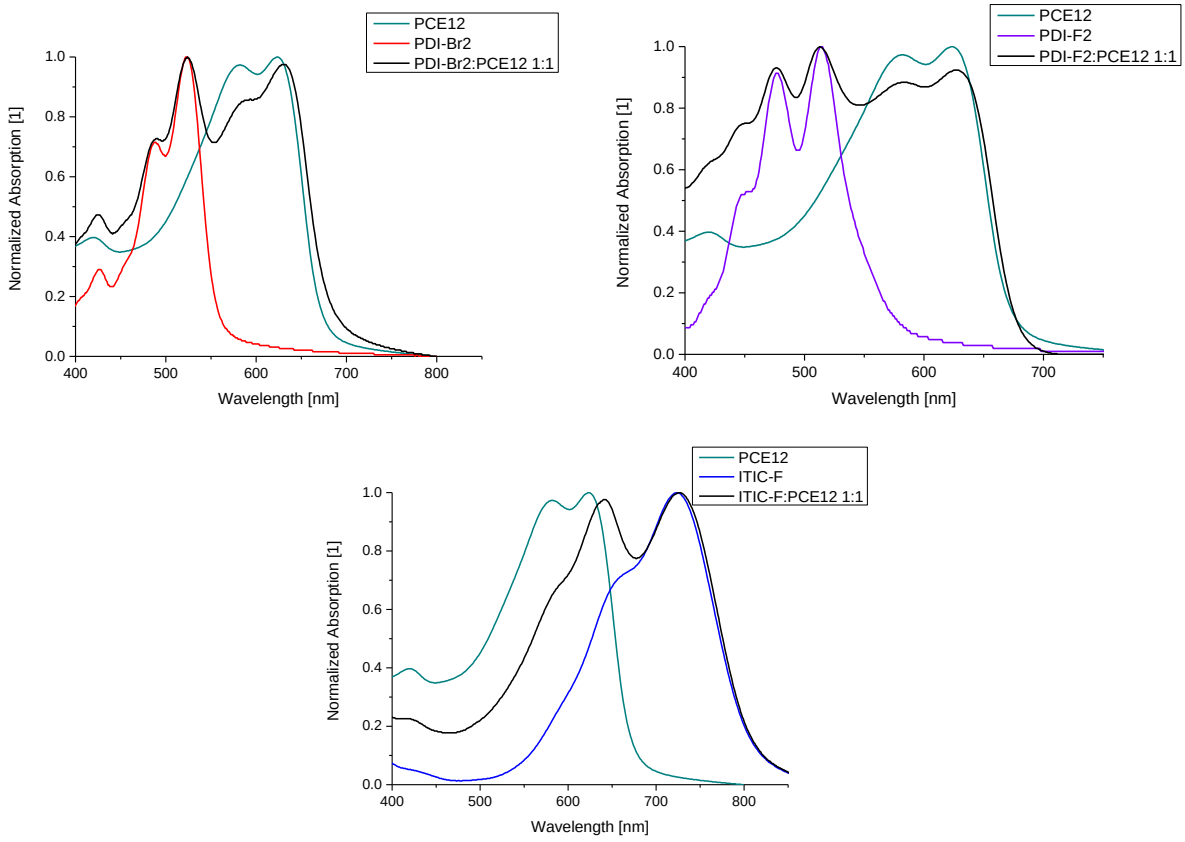

Figure 29: Absorption spectra of each acceptor, the donor and the blend of both. PDI-Br_2 (top left), PDI-F_2 (top right) and ITIC-F (bottom); in red PDI-Br_2, purple PDI-F_2, blue ITIC-F, turquoise PCE12 and in black the blend

PCE12 has its absorption maxima between 500 and 700 nm. The acceptors, however, work best at 400 to 600 nm (PDI-Br_2 and PDI-F_2) and 550 to 800 nm (ITIC-F). As expected, the donor and acceptor blend gave an absorption range of 450 to 700 nm for PDI-Br_2 and PDI-F_2 and 500 to 800 nm for ITIC-F.

Figure 30 shows the external quantum efficiency (EQE) of the donor and acceptor blends of the best cells of all three acceptor materials. In the left spectra all acceptors are depicted; on the right only PDI-Br_2 and PDI-F_2 are shown for easier comparison reasons.

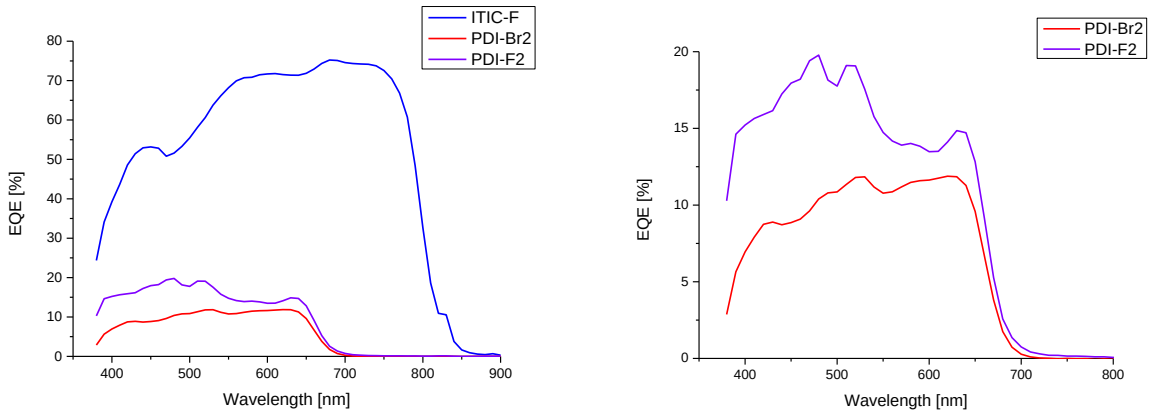

Figure 30: EQE measurement of the solar cell devices. ITIC-F in blue, PDI-Br_2 in red and PDI-F_2 in purple.

The EQE for ITIC-F, as excepted, showed higher values as the other two PDI derivatives. When compared to the absorption spectra of each of the blends, the EQE curves looked similar. Between both PDI derivatives, PDI-F_2 showed higher EQE values. The IV characteristics, which were measured before the EQE measurement, stayed the same afterwards for all of the materials. Additionally, light soaking experiments for each acceptor/donor blend was done for 15 min and IV characteristics were measured again. No change could be noticed after light soaking for neither of the donor/acceptor blends.

Additionally, the influence of the annealing temperature on the assembled solar cells was tested (Figure 31). Therefore each solar cell was annealed at a certain temperature (starting at 60°C). Each annealing step was done for 10 min.

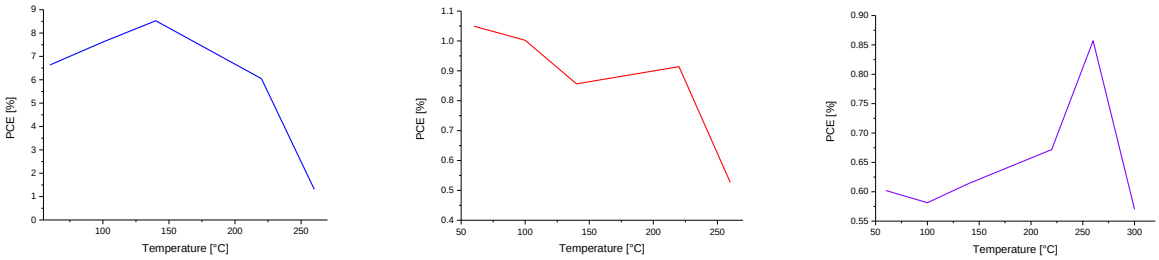

Figure 31: Influence of temperature on the assembled solar cells. In blue ITIC-F, red PDI-Br_2 and purple PDI-F_2

Solar cells with ITIC-F as acceptor material show an increase in PCE from 60 °C to 140 °C. After 140 °C the efficiency decreased drastically. For PDI-Br an increased annealing temperature showed a negative effect. PDI-F_2 showed the complete opposite behavior than PDI-Br_2. With an increase in annealing temperature the PCE was increased as well. At 220 °C a maximum is reached and at 300 °C the solar cell did not work properly anymore. In comparison to the other acceptor materials, PDI-F_2 could undergo the highest temperature. PDI-Br_2 and ITIC-F solar cells stopped working properly at 220 °C. It can be assumed that PCE12 is evaporating (T_g = 105-210 °C[82]) and therefore, the efficiency is starting to decrease. Additionally, the active layer can diffuse in the electrode materials at high temperatures, resulting in a decrease in efficiency.

5 Experimental

5.1 Chemicals and Materials

Table 11: List of chemicals used for synthesis and assembly of solar cells

Chemicals	Purity Grade / Description	Supplier
Bromine, Br_2	> 99 %, iodometric	Merck
Iodine, I_2	99.99 % (trace metal basis), pellets	Sigma Aldrich
Perylene-3,4,9,10-tetracarboxylic dianhydride, PTCDA	>98.0%	TCI
Sulfuric acid, H_2SO_4	> 95 %	Fisher Scientific
Propionic acid, CH_3CH_2COOH	99 %	Sigma Aldrich
2,6-diisopropylaniline, $H_2NC_6H_3(CH(CH_3)_2)_2$	97 %	Sigma Aldrich
Potassium fluoride, KF	99 %	Fluka
18-crown-6	FCB081436	Fluorochem
Sulfolane, $C_4H_8O_2S$	99.0 %	Merck
Cuprous cyanide, CuCN	≥ 99.0 %	Fluka
Dimethylformamide, DMF	≥ 99.8 %	Sigma Aldrich
Tetrakis(triphenylphosphine)-Palladium, $Pd(PPh_3)_4$	99.9 %	abcr
Ethanol, EtOH	96 %	TU Graz
Aliquat 336	Highly viscous liquid	Sigma Aldrich
Toluene	99.5 %	TU Graz
Chlorobenzene, CB	99.8 %, anhydrous	Sigma Aldrich
Chloroform, CF	≥ 99.9 %	Sigma Aldrich
Dichloromethane, DCM	99.8 %	Fisher Scientific
Molybdenum(II)oxide	99.98 % (trace metal basis)	Sigma Aldrich
Silver, Ag	99.99 %, pellets	Kurt J. Lesker Company
PBDB-T/PCE-12	OS0804	One Material
Zinc acetate dehydrate	≥ 99.5 %	Fluka
2-Methoxyethanol	99.8 %, anhydrous	Sigma Aldrich
Ethanolamine	≥ 99 %	Sigma Aldrich
Methanol, MeOH	100 %	VWR

5.2 Synthesis

Most of the reactions were done under nitrogen atmosphere. This was achieved by a constant stream of nitrogen gas throughout the whole reactions. Additionally, a balloon filled with nitrogen gas was used before the reaction started to degas the solvents, as well as the reaction mixtures.

All the reactions needed to be heated up. Therefore a silicon oil bath was used.

5.2.1 Analytical Methods

5.2.1.1 Flash Chromatography

Silica gel 60 (particle size 0.06 – 0.2mm) from Macherey-Nagel was used. The products were either dissolved in the appropriate solvent or dissolved and absorbed on silica gel before applying on the column.

5.2.1.2 Thin Layer Chromatography (TLC)

Thin layer chromatography was used to observe the reaction, as well as to identify the purity of the product mixture. Silica gel plates (Silica gel 60 F_{254} from Merck Millipore) were used.

5.2.1.3 Mass Spectrometry (MS)

Mircromass MALDI micro MX mass spectrometer by Waters was used for the measurement. As a matrix Dithranol in a concentration of 10 mg/mL in THF was used. The concentration of the sample was 1 mg/mL in DCM in a mixing ratio matrix/sample = 7/2. As a reference material polyethylene glycol (PEG) was used. The measurement was performed by Karin Bartl. Data analysis was performed with MassLynx V4.1 software.

5.2.1.4 Nuclear Magnetic Resonance Spectroscopy (NMR)

NMR spectra were done on a Bruker Advance III (300 MHz) with auto sampler, as well as on an Inova 500 (500 MHz) spectrometer. Measurements on the Inova 500 spectrometer were executed by Petra Kaschnitz.

5.2.1.5 Fluorescence Spectroscopy

3 samples in $CHCl_3$ were prepared with a maximum absorption smaller than 0.1. Therefore, a UV/VIS spectrum was recorded for each sample before the fluorescence measurement for reassurance. The spectra were recorded on a UV-Visible Spectrophotometer Cary 50 Conc by Varian. Settings are listed in Table 12.

Table 12: Settings for the absorption measurement in $CHCl_3$

Start wavelength [nm]	800
End wavelength [nm]	350
Slit width [nm]	1.0
Scan speed [nm/s]	70

For the fluorescence spectra a FluoroLog 3 spectrofluorometer from Horiba Scientific Jobin Yvon adjusted with R2658 photomultiplier from Hamamatsu was used. As reference material "Fluoreszenzorange" in $CHCl_3$ was chosen. The settings can be seen in Table 13.

Table 13: Settings for the fluorescence measurement in $CHCl_3$

	PDI-Br_2	**PDI-F_2**
Start wavelength [nm]	500	490
End wavelength [nm]	800	800
Slit width [nm]	1.0	1.0
Excitation wavelength [nm]	490	480

5.2.1.6 UV/VIS Spectroscopy and Optical Band Gap Determination in Solution

UV/VIS spectra in chloroform were done with a UV spectrophotometer 'UV-1800' from Shimadzu. All the measurements were done 3x to achieve reproducible results. Each vial contained about 1 mg product which was dissolved in 10 mL chloroform (1:1). 1 mL was taken out and diluted with 9 mL $CHCl_3$ (1:10). Out of this vial, again 1 mL was taken out and diluted with 9 mL chloroform (1:100). The following settings were used.

Table 14: Settings for the absorption measurement in $CHCl_3$

Start wavelength [nm]	800
End wavelength [nm]	350
Slit width [nm]	1.0
Scan speed [nm/min]	350
Data interval [nm]	1

The extinction coefficient was determined for each material with the accurate concentrations, as well as the absorbance maxima. Also the band gap out of the absorption spectra was determined.

5.2.1.7 Thermogravimetric Analysis (TGA)

TGA coupled with differential scanning calorimetry (DSC) was done with a STA 449 C by NETSCH. Each sample was measured in an aluminium pan with helium as protective gas with a flow rate of 50 mL/min. Heating rate was 10 K/min. The samples were measured from 20-550 °C. Measurements were performed by Josefine Hobisch.

5.2.2 Experimental Procedures

5.2.2.1 5,12-dibromo-2,9-bis(2,6-diisopropylphenyl)anthra[2,1,9-def:6,5,10-d'e'f']diisoquinoline-1,3,8,10(2H,9H)-tetraone

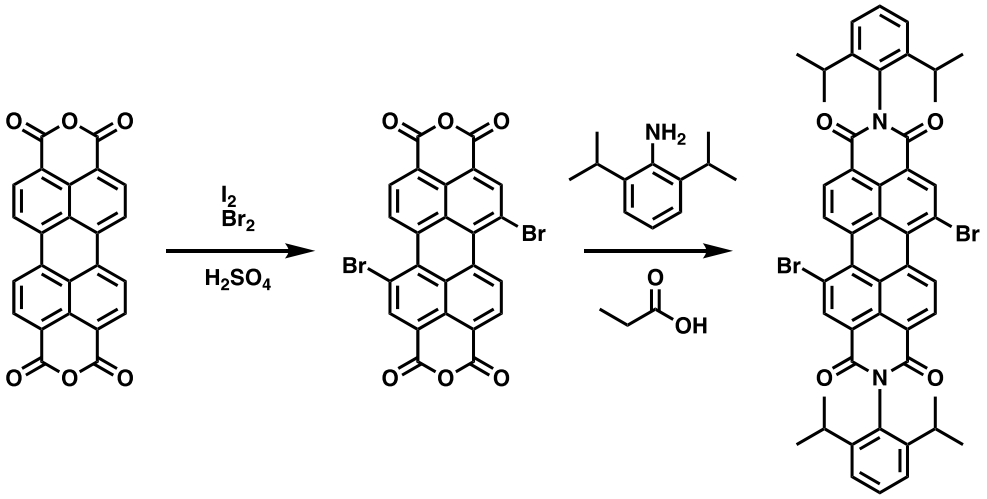

Scheme 6: Synthesis of PDI-Br$_2$

^{1}H-NMR (500 MHz; $CDCl_3$) δ = 9.60 (2H, d, $^3J_{HH}$=7.8 Hz), 9.02 (2H, s), 8.80 (2H, d, $^3J_{HH}$=7.8 Hz), 7.52 (2H, t, $^3J_{HH}$=7.8 Hz), 7.38-7.36 (4H, d, $^3J_{HH}$=7.8 Hz), 2.74 (4H, m, $^3J_{HH}$=7.0), 1.20-1.18 (24H, d, $^3J_{HH}$=7.2)

Orange-red powder; yield was not possible to determine

First Reaction

10.01 g perylene-3,4;9,10-tetracarboxylic acid dianhydride (PTCDA) was suspended in 300 mL concentrated sulfuric acid and stirred for 1 hour. 0.552 g iodine and 8 mL bromine was added. The mixture was stirred for 3 days. The finished reaction mixture was slowly transferred into distillated water and filtrated. The solid product was washed with distilled Water until the pH-value was neutral.

For the second step 14.03 g PTCDA-Br_2 and 19 mL 2,6-diisopropylaniline were dissolved in a 500mL two-neck-flask and 400 mL propionic acid. The reaction was refluxed under nitrogen atmosphere for three days. After cooling to room temperature the reaction mixture was poured on 700 mL distilled water and the precipitate was filtrated. The product was dissolved in CH_2Cl_2 and dried with Na_2SO_4. The solvent was evaporated under reduced pressure. The product was purified by flash chromatography with CH_2Cl_2.

Second Reaction

506 mg of PTCDA was dissolved in 4mL conc. H_2SO_4 in a three-neck-flask. The solution was stirred at room temperature under an air atmosphere for two days. 12 mg of I_2 and 170 μL of Br_2 were added to the solution. The solution was heated to 85°C overnight under vigorous stirring. On the next day the mixture was cooled to room temperature and the product was isolated by filtration as well as washed with distilled water until the pH value reached 7.

All of the product of the first step of the reaction and 0.98 mL 2,6-diisopropylaniline were dissolved in a 100 mL three-neck-flask with 40 mL propionic acid. The reaction was refluxed under nitrogen atmosphere for 24 hours. The reaction mixture was cooled to room temperature and poured onto 40 mL distilled water. The precipitate was filtrated and solved in CH_2Cl_2. Separation of the two phases was done in a separation funnel (3x CH_2Cl_2). The organic phase was dried with Na_2SO_4 as well as filtrated afterwards. The solvent was evaporated under reduced pressure. Purification was done by recrystallization steps with CH_2Cl_2 and MeOH for ten times.

Third Reaction

Because more product of the PDI-Br_2 was needed, the reaction was done again with the same conditions as previous reactions. 5 g starting material was used.

5.2.2.2 2,9-bis(2,6-diisopropylphenyl)-5,12-difluoroanthra[2,1,9-def:6,5,10-d'e'f']diisoquinoline-1,3,8,10(2H,9H)- tetraone

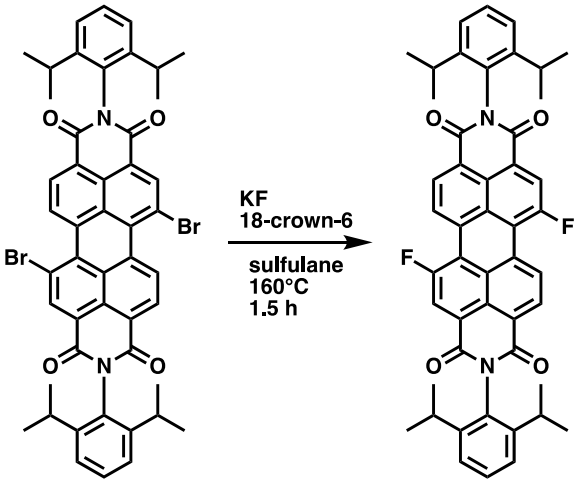

Scheme 7: Synthesis of PDI-F_2

^{1}H-NMR (500 MHz; $CDCl_3$) δ = 9.25 (dd, 2H, $^3J_{HH}$=6.0, $^3J_{HH}$=5.0 Hz), 8.83 (d, 2H, $^3J_{HH}$=9.2 Hz), 8.64 (d, 2H, $^3J_{HH}$=13.5 Hz), 7.52 (t, 2H, $^3J_{HH}$=7.7 Hz), 7.37-7.36 (d, 4H, $^3J_{HH}$=7.7 Hz), 2.74 (m, 4H, $^3J_{HH}$=7.1 Hz), 1.20-1.18 (d, 24H, $^3J_{HH}$=6.5 Hz)

Orange-yellow powder; yield: 54%

First Reaction

100 mg PDI-Br_2, KF and 5 mL18-crown-6 (wrong calculation; 0.005 mL or 6.08 mg) were put in a 50 mL one-neck-flask and were dissolved in 0.7 mL sulfolane. The reaction mixture was heated to 160-170 °C for 1.5 h under vigorous stirring. The resulting product was cleaned with flash chromatography two times (DCM:MeOH = 50:1 and DCM:MeOH = 200:1).

Second Reaction

The second reaction was done like the first one with the same amount of starting material. Only difference was the usage of the isolated 1,7-isomer of PDI-Br_2 and the proper amount of 18-crown-6.

5.2.2.3 2,9-bis(2,6-diisopropylphenyl)-1,3,8,10-tetraoxo-1,2,3,8,9,10-hexahydroanthra[2,1,9-def:6,5,10-d'e'f']diisoquinoline-5,12-dicarbonitrile

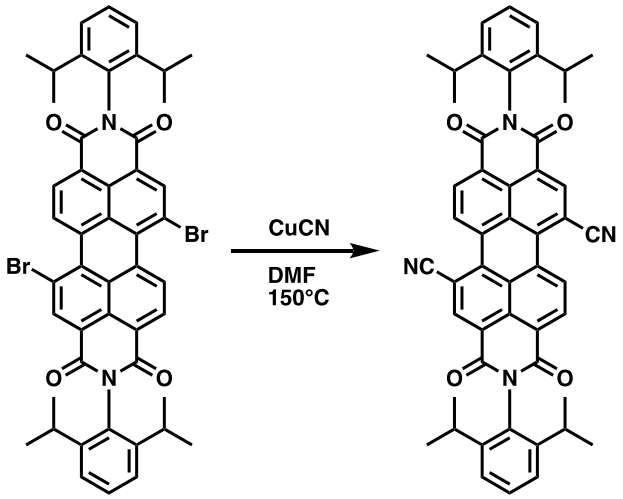

Scheme 8: Synthesis of PDI-$(CN)_2$

^{1}H-NMR (500 MHz; $CDCl_3$) δ = 9.73-9.73 (d, 2H, $^3J_{HH}$=7.8 Hz), 9.08 (s, 2H), 9.04-9.01 (d, 2H, $^3J_{HH}$=7.8 Hz), 7.57-7.52 (d, 2H, 7.6 Hz), 7.39-7.36 (d, 4H, $^3J_{HH}$=7.6 Hz), 2.7 (m, 4H, 6.7 Hz), 1.20-1.18 (d, 27H, 6.7 Hz)

MS (MALDI/TOF) m/z: 762.3297 (calculated for $C_{50}H_{40}N_4O_4$, $[MH]^+$ 761.3050)
Red powder; yield: 10%

First Reaction

To a 100 mL round bottom flask 108 mg of PDI-Br_2 and 250 mg CuCN were dissolved in. 6 mL of DMF was added and the mixture was heated under vigorous stirring at 150°C under N_2 atmosphere for 6 h. The mixture was cooled down overnight.

The reaction mixture then was continuously Soxhlet extracted with DCM over three days, followed by evaporation until dryness. The product was filtrated and flash chromatography with DCM:MeOH (100:1 and 50:1; gradient chromatography) was performed.

Second Reaction

The second reaction was done exactly in the same way as the first one with the same amount of starting material. Only difference was the usage of the isolated 1,7-isomer of PDI-Br_2.

5.2.2.4 2,9-bis(2,6-diisopropylphenyl)-5-(2-(2,6-diisopropylphenyl)-1,3-dioxo-2,3-dihydro-1H-benzo[10,5]anthra[2,1,9-def]isoquinolin-8-yl)-12-(2-(2,6-diisopropylphenyl)-12-methyl-1,3-dioxo-2,3-dihydro-1H-benzo[10,5]anthra[2,1,9-def]isoquinolin-8-yl)anthra[2,1,9-def:6,5,10-d'e'f']diisoquinoline-1,3,8,10(2H,9H)-tetraone

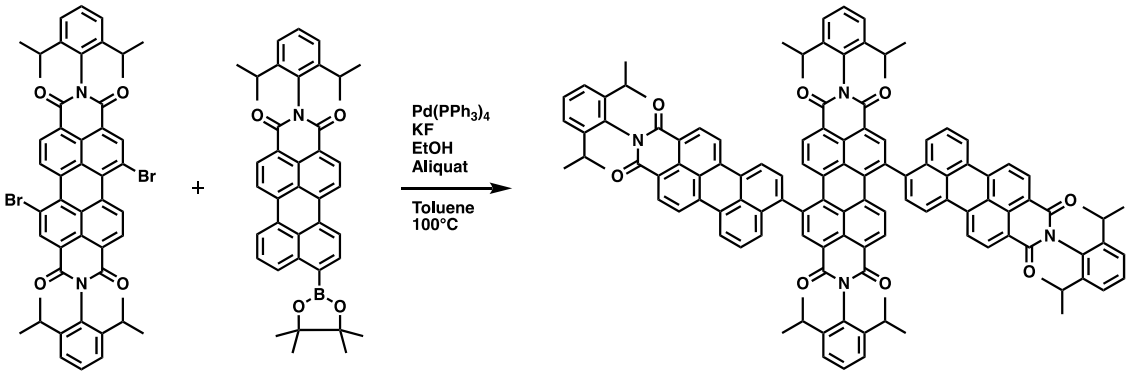

Scheme 9: Synthesis of PDI-$(PMI)_2$

Dark red, almost black powder; yield was not possible to determine

First Reaction

207.6 mg of PDI-Br_2 and 369.0 mg of PMI-boronic acid, pinacol ester were added to a 3-neck-flask (100 mL). 40 mL toluene, 3 mL KF (1M), 0.3 mL EtOH, as well as 1 drop of Aliquat were added to the mixture and stirred under N_2 (air balloon) for approximately 5 min. 1 spatula of $Pd(PPh_3)_4$ was added and the mixture was again stirred under N_2 (air balloon) for another 5 min. Afterwards the reaction mixture was heated until reflux (100 °C) for 48 h. The reaction was controlled via TLC. After the reaction finished, the mixture was put in a separation funnel (2x dest.

H_2O, 2x toluene, 2x brine) and the organic phase was dried over Na_2SO_4. The resulting product was purified with flash chromatography (DCM) and recrystallization (DCM/MeOH).

Second Reaction

The second reaction was done exactly in the same way as the first one. Only difference was the usage of the isolated 1,7-isomer of PDI-Br_2.

5.3 Organic Solar Cells

5.3.1 General Procedure

The Assembly of the organic solar cells in this work was done in an inverted architecture with a bulk heterojunction design. The device consists of a top electrode (Ag), active layer (PDI derivative as acceptor and PCE12 as donor material) and the bottom electrode (ITO) on a glass substrate with interlayers (ZnO, MoO_3). The assembly was achieved according to the following procedure.

5.3.1.1 Cleaning/Activation of the Substrates

Glass substrates (ITO coated) of 15 x 15 x 1.1 mm with a sheet resistance of 15 Ω (purchased from Luminescencce Technology Corporation) were cleaned with water and acetone before they were put in a bath of 2-propanol at 40 °C for ultrasonic treatment (Ultrasonic Cleaner from VWR). After the treatment the substrates were individually dried with compressed air (N_2), followed by plasma etching at a constant oxygen gas flow for 3 min (Femto etcher by Diener Electronics). After the cleaning and activation step the substrates were transferred into the N_2-filled glove box (LabMaster dp by MBraun).

5.3.1.2 ZnO-Interlayer

A sol-gel procedure was done for the application of the ZnO-interlayer. Therefore, a precursor solution with a composition of 500 mg zinc acetate dehydrate, 5 mL 2-methoxyethanol, as well as 150 µL ethanolamine was prepared and mixed, as well as stirred outside the glove box for approximately 18 h. The solution was then transferred into the glove box and stirred again. Each substrate was then coated with the ZnO-interlayer by spin coating 35 µL of the precursor solution

with 4000 rpm and 2000 rpm/s acceleration for 30 s (layer thickness between 20 and 30 nm). For the spin coating a spin coater from Laurell Technologies (Model WS-650MZ-23NPPB) was used. After this procedure the substrates were annealed at 150 °C outside the glove box for about 10min and transferred back inside again.

5.3.1.3 Active Layer

The used acceptor materials (PDI-Br_2, PDI-F_2, PDI-$(CN)_2$ and ITIC-F) were diluted with chlorobenzene and dissolved for approximately one hour at 50 °C. As a donor material PCE-12 was added and the mixture was stirred overnight at 50 °C. The concentration for all was 10 mg/mL and the Donor/Acceptor-ratio was 1:1. The resulting solution was spin coated on the substrates with different parameters to obtain a layer thickness of 100 nm. For each substrate a drying step was added in the spin coating process with 4000 rpm, 4000 acc. For 5 s. After the deposition of the active layer, different annealing steps with varying temperature for 10 min were done.

5.3.1.4 MoO_3-Interlayer and Ag-Electrode

The MoO_3-interlayer (10 nm), as well as the Ag-electrode (100 nm) were deposited on each substrate by thermal evaporation. For this step, a shadow mask was used to achieve an electrode area of 0.09 cm^2. Evaporation was done under at least 1 x 10^{-5} mbar.

5.3.2 Characterization

5.3.2.1 UV/VIS-Spectroscopy in Films

UV/VIS-Sepctroscopy was recorded with an UV/VIS-Spectrometer Lambda 35 from Perkin Elmer. The settings can be seen in Table 15.

Table 15: Settings for the absorption measurement of acceptor, donor and blend in films.

Start wavelength [nm]	800
End wavelength [nm]	400
Slit Witdh [nm]	1.0
Scan Speed [nm/min]	240
Data Interval [nm]	1

The absorption spectra were measured in thin films on glass substrates. These films of the acceptor, donor, as well as the blend (D:A = 1:1) of both were spin coated on a glass substrate and had a concentration of 10 mg/ml. The used solvent was chlorobenzene. The preparation was done in a N_2-filled glove box.

5.3.2.2 IV- Characteristics

For the measurement a Keithley 2400 SourceMeter, a custom-made Lab-view software and as a light source a Dedolight DEB400D lamp (intensity: 100 mW/cm^2) was used. The settings can be found in Table 16.

Table 16: Settings for IV-measurements

Start [mV]	1500
End [mV]	-500
Compliance [mA]	100
Number of points	100
Overwrite max compliance [mA]	500
Delays [ms]	100
Step widths [V]	-0.02

The IV curves were monitored under illumination, as well as dark conditions for each solar cell. The active area of each solar cell was 0.09 cm^2. A shadow mask was used for all measurements with an active area of 0.070225 cm^2.

5.3.2.3 Layer Thickness and Roughness

To determine the layer thickness and roughness a contact profilometer DektakXT from Bruker was used. Therefore, a small scratch with a blade was applied to analyze the thickness and roughness of the active layer (5 different positions).

5.3.2.4 External Quantum Efficiency (EQE)

To determine the external quantum efficiency an IPCE (incident photon-tocurrent efficiency) measuring system was used. It consists of a MuLTImode 4-AT monochromator by Amko with a xenon lamp (LPS 210-U by Amko), as well as a Keithley 2400 SourceMeter. The measurements were carried out for the best solar cell of each acceptor. Therefore the solar cell was sealed under

N_2 in a custom made measuring box. Calibration with a photo diode (1.2 mm) has to be done before the EQE-spectra were monitored (380-900 nm).

5.3.2.5 Light microscopy

The light microscope BX60 from Olymp with an attached camera (Olymp) was used to get images of the active layer from the solar cell devices. The images have a magnification of 500x.

6 Summary and Conclusion

In this work, two out of four desired perylene derivatives (1,7-bromine and 1,7-fluorine derivative) as acceptor materials were successfully synthesized with yields ranging from 10 to 54%, which is much lower than in literature. It can be assumed, that the lower yields come from the formation of many different side-products, as well as product loss during purification (flash chromatography, thin layer chromatography). Further optimization of the different reactions and their conditions could be done to achieve higher yields. Additionally, some fractions were still not purified yet and therefore reduce the yield as well. The other two acceptor materials needed further purification steps and still showed in the NMR-spectra side products. All of the products showed perfect solubility in dichloromethane, chloroform, chlorobenzene and toluene. Therefore, all products were suitable for the assembly in organic solar cells.

The absorption maxima of the different synthesized PDI derivatives were measured. When compared to PDI, PDI-Br_2 showed almost the same absorption maxima of 521 nm. Only a very slight shift to longer wavelength was noticeable. PDI-F_2, however, showed a visible shift to a smaller wavelength. The absorption maxima for this derivative was around 510 nm. The molar absorption coefficient for the fluorine derivative was higher when compared with PDI-Br_2 and exhibited a value of 91 000 L mol^{-1} cm^{-1}. PDI-Br_2 reached a value of 71 500 L mol^{-1} cm^{-1}. These values are affected by the effect of a rather flat perylene core instead of a twisted one. The values for the optical bandgap offered similar results for both of the derivatives with a difference of only 0.1 eV. When compared with DFT calculations, the achieved experimental data showed reasonable values. The calculated bandgap showed a difference of only 0.01 eV and the absorption maxima also exhibited a higher value for the bromine derivative.
The fluorescence spectra showed similar behavior for both compounds, however the Stokes shift was quite different when compared with 28.0 nm for PDI-Br_2 and 8.2 nm for PDI-F_2. The calculated quantum yield was similar for both derivatives.
Thermal analysis (TGA coupled with DSC) of both derivatives showed a high melting point for the fluorine derivative at 414 °C. No melting point for PDI-Br_2 was observed. However, both of the derivatives showed a high thermal stability and decomposed at high temperature. The overall mass loss after decomposition for both products was almost identical.

After optical and thermal characterization, the different derivatives were assembled in solar cells. Different annealing temperatures before the thermal evaporation of Ag and MoO_3 were tried out. For ITIC-F, as well as PDI-Br_2 the PCE increased with higher annealing temperatures. However, for PDI-F_2 it increased at first, but decreased at high temperatures.

The acceptor which exhibits the best efficiency between the synthesized PDI derivatives, at first, was PDI-F_2. After three days, a second annealing behavior experiment for each cell with the highest efficiency was performed. Therefore, the already assembled solar cells were annealed until their PCE decreased. Here, PDI-Br_2 showed the higher PCE after three days in general. Even after annealing temperatures, the PCE values for PDI-Br_2 was higher than for the fluorine derivative. Therefore, PDI-F_2 as an acceptor material was not as stable as the bromine derivative. Both PDI derivatives were completely soluble in chlorobenzene. However, light microscopy showed that crystallites on some of the substrates of PDI-F_2 based solar cells were formed. However, these devices showed the highest PCE, whereas the substrates with no crystallites offered quite low efficiencies.

When compared to ITIC-F, both PDI derivatives showed pour values in aspect of fill factor and efficiency. Therefore, further optimization of the donor/acceptor ratio, the concentration and the annealing temperature needs to be done in future. To learn more about the morphology of the different PDI derivatives, electron microscopy, for example atomic force microscopy, needs to be done. Also the films could be investigated via grazing-incident x-ray scattering methods.

7 References

(1) Ritchie H.; Roser M.; Fossil fuels. https://ourworldindata.org/fossil-fuels. (accessed Jan 23, 2020)

(2) Global energy & CO2 status report 2019. https://www.iea.org/reports/global-energy-and-co2-status-report-2019 (accessed Jan 23, 2020)

(3) Solar panel brief history and overview. https://www.energymatters.com.au/panels-modules/ (accessed Jan 23, 2020)

(4) Haegel N. M.; Margolis R.; Buonassisi T.; Feldman D.; Froitzheim A.; Garabedian R.; Green M.; Glunz S.; Henning H.-M.; Holder B.; Kaizuka I.; Kroposki b.; Matsubara K.; Niki S.; Sakurai K.; Schinderl R. A.; Tumas W.; Weber E. R.; Wilson G.; Woodhouse M.; Kurtz S.; Terawatt-scale photovoltaics: trajectories and challenges. Science. 2017, 356, 141-143

(5) Solar generation 6 – solar photovoltaic electricity empowering the world. https://web.archive.org/web/20120822034710/http://www.epia.org/publications/epiapublications/solar-generation-6.html (accessed Jan 23, 2020)

(6) Glunz S. W.; Preu R.; Biro D.; 1.16 – Crystalline silicon solar cells: state-of-the-art and future developments. Comprehensive Renewable Energy. 2012, 1, 353-387

(7) Helmholtz-Zentrum Berlin für Materialien und Energie; Boosting the efficiency of silicon solar cells. ScienceDaily. 2018. www.sciencedaily.com/releases/2018/10/181004112555.htm (accessed Jan 23, 2020)

(8) Akihiro K.; Kenjiro T.; Yasuo S.; Tsutomu M.; Organometal halide perovskites as visible-light sensitizers for photovoltaic cells. Journal of the American Chemical Society. 2009, 131, 6050-6051

(9) Utama K. F.; Ducati C..; Characterising degradation of perovskite solar cells through in-situ and operando electron microscopy. Nano Energy. 2018, 47, 243-256

(10) Askari M. B.; Introduction to Organic Solar Cells. Sustainable Energy. 2014, 2, 85

(11) Best research-cell efficiency chart. 2019. https://www.nrel.gov/pv/cell-efficiency.html (accessed Feb 3, 2020)

(12) H. Zhang H.; Yao H.; Hou J.; Zhu J.; Zhang J.; Li W.; Yu R.; Gao B.; Zhang S.; , Hou J.; Over 14% efficiency in organic solar cells enabled by chlorinated nonfullerene small-molecule acceptors". Adv. Mater.; 2018, 30, e1800613

(13) Meng L.; Zhang Y.; Wan X.; Li C.; Zhang X.; Wang Y.; Ke X.; Xiao Z.; Ding L.; Xia R.; Yip H. L.; Cao Y.; Chen Y.; Organic and solution-processed tandem solar cells with 17.3% efficiency. Science. 2018, 361,1094-1098

(14) Duan L.; Elumalai N. K.; Zhang Y; Uddin A.; Progress in non-fullerene acceptor based organic solar cells. Solar Energy Materials and Solar Cells. 2019, 193, 22-65

(15) Rodriquez D.; Savagatrup S.; Valle E.; Proctor C. M.; McDowell C.; Bazan G. C.; Nguyen T. Q.; Lipomi D. J.; Mechanical properties of solution-processed small-molecule semiconductor films. ACS Appl. Mater. Interfaces. 2016, 8, 11649-11657

(16) Delgado J. L.; Bouit P.-A.; Filippone S.; Herranz M. A.; Martin N.; Organic photovoltaics: a chemical approach. Chemical Communications. 2010, 27, 4853-4865

(17) W. Zhao et al.; Molecular Optimization Enables over 13% Efficiency in Organic Solar Cells. J. Am. Chem. Soc. 2017, 139, 21, 7148-7151.

(18) Li S.; Ye L.; Zhao W.; Yan H.; Yang B.; Liu D.; Li W.; Ade H.; Hou J.; A wide band-gap polymer with a deep HOMO level enables 14.2% efficiency in polymer solar cells. J. Am. Chem. Soc. 2018, 140, 7159-7167

(19) Rivers P. N.; (2007). Leading edge research in solar energy. Nova Science Publishers. ISBN 978-1600213366.

(20) Sauve G.; Fernando R.; Beyond fullerenes: designing alternative molecular electron acceptors for solution-processable bulk heterojunction organic photovoltaics. J. Phys. Chem. Lett. 2015, 6, 18, 3770-3780

(21) Mazzio K. A.; Luscombe C. K.; The future of organic photovoltaics. Chemical Society Reviews. 2015, 44, 78-90

(22) Sariciftci N. S.; Smilowitz L.; Heeger A. J.; Wudl F.; Photoinduced electron transfer from a conducting polymer to buckminsterfullerene. Science. 1992, 258, 1474-1476

(23) Marinova N.; Velero S.; Delgado J. L.; Organic and perovskite solar cells: working principles, materials and interfaces. Journal of Colloid and Interface Science. 2017, 488, 373-389

(24) Nelson J.; Organic photovoltaic films. Current Opinion in Solid State and Materials Science. 2002, 6, 87-95

(25) Hoppe H.; Sariciftci N. S.; Organic solar cells: an overview. Journal of Materials Research. 2004, 19, 1924-1945

(26) Halls J. J. M.; Friend R. H.; Archer M. D.; Hill R. D.; Clean electricity from photovoltaics. ISBN 978-1860941610

(27) McGehee M.; Topinka M.; Pictures from the blended zone. Nature Mater. 2006, 5, 675–676

(28) Cao W.; Xue J.; Recent progress in organic photovoltaics: device architecture and optical design. Energy & Environmental Science. 2014, 7, 2123-2144

(29) Heeger A. J.; 25th anniversary article: Bulk heterojunction solar cells: understanding the mechanism of operation. Advanced Materials. 2013, 26, 10-28

(30) Scharber M. C.; Sariciftci N. S.; Efficiency of bulk-heterojunction organic solar cells. 2013, 38, 1929-1940

(31) Yin Z.; Wei J.; Zheng Q.; Interfacial materials for organic solar cells: recent advances and perspectives. Advanced Science. 2016, 3

(32) White M. S.; Olson D. C.; Shaheen S. E.; Kopidakis N.; Ginley D. S.; Inverted bulk-heterojunction organic photovoltaic device using a solution-derived ZnO underlayer. Appl. Phys. Lett. 206, 89, 143517

(33) Waldauf C.; Morana M.; Denk P.; Schilinsky P.; Coakley K.; Choulis S. A.; Brabec C. J.; Highly efficient inverted organic photovoltaics using solution based titanium oxide as electron selective contact. Appl. Phys. Lett. 2006, 89, 233517

(34) Siddiki M. K.; Venkatesan S.; Qiao Q.; Nb2O5 as a new electron transport layer for double junction polymer solar cells. Physical Chemistry Chemical Physics. 2012, 14, 4682-4686

(35) Trost S.; Zilberberg K.; Behrendt A.; Riedl T.; Room-temperature solution processed SnOx as an electron extraction layer for inverted organic solar cells with superior thermal stability. Journal of Materials Chemistry. 2012, 22, 16224-16229

(36) Huang J.; Yin Z.; Zheng Q.; Applications of ZnO in organic and hybrid solar cells. Energy & Environmental Science. 2011, 4, 3861-3877

(37) Chen S.; Manders J. R.; Tsang S.-W.; So F.; Metal oxides for interface engineering in polymer solar cells. Journal of Materials Chemistry. 2012, 22, 24202-24212

(38) Yip H.-L.; Jen A. K.-Y; Recent advances in solutionprocessed interfacial materials for efficient and stable polymer solar cells. Energy & Environmental Science. 2012, 5, 5994-6011

(39) Yin Z.; Zheng Q.; Chen S.-C.; Cai D.; Interface control of semiconducting metal oxide layers for efficient and stable inverted polymer solar cells with open-circuit voltages over 1.0 Volt. ACS Appl. Mater. Interfaces. 2013, 5, 9015-9025

(40) Jasieniak J. J.; Seifter J.; Jo J.; Mates T.; Heeger A. J.; A solution-processed MoOx anode interlayer for use within organic photovoltaic devices. Advanced Functional Materials. 2012, 22, 2594-2605

(41) Xie F.; Choy W. C. H.; Wang C.; Li X.; Zhang S.; Hou J.; Low-temperature solution-processed hydrogen molybdenum and vanadium bronzes for an efficient hole-transport layer in organic electronics. Advanced Materials. 2013, 25, 2051-2055

(42) Tremolet de Villers B. J.; MacKenzie R. C. I.; Jasieniak J. J.; Treat N. D.; Chabinyc M. L.; Linking vertical bulk-heterojunction composition and transient photocurrent dynamics in organic solar cells with solution-processed MoO_x contact layers. Advanced Energy Materials. 2013, 4, 1301290

(43) Tan Z.; Quian D.; Zhang W.; Li L.; Ding Y.; Xu Q.; Wang F.; Li Y.; Efficient and stable polymer solar cells with solution-processed molybdenum oxide interfacial layers. Journal of Materials Chemistry A. 2013, 1, 657-664

(44) Stubhan T.; Li N.; Luechinger N. A.; Halim S. C.; Matt G. J.; Brabec C. J.; High fill factor polymer solar cells incorporating a low temperature solution processed WO3 hole extraction layer. Advanced Energy Materials. 2012, 2, 1433-1438

(45) Wang K.; Ren H.; Yi C.; Liu C.; Wang H.; Huang L.; Zhang H.; Karim A.; Gong X.; Solution-processed Fe3O4 magnetic nanoparticle thin film aligned by an external magnetostatic field as a hole extraction layer for polymer solar cells. Applied Materials & Interfaces. 2013, 5, 10325-10330

(46) Zhang J.; Wang J.; Fu Y.; Zhang B.; Xie Z.; Sonochemistry-synthesized CuO nanoparticles as an anode interfacial material for efficient and stable polymer solar cells. RSC Advances. 2015, 5, 28786-28793

(47) Wang F.; Xu Q.; Tan Z.; Li L.; Li S.; Hou X.; Sun G.; Tu X.; Hou J.; Li Y.; Efficient polymer solar cells with a solution-processed and thermal annealing-free RuO2 anode buffer layer. Journal of Materials Chemistry A. 2014, 2, 1318-1324

(48) Tu X.; Wang F.; Li C.; Tan Z.; Li Y.; Solution-processed and low-temperature annealed CrOx as anode buffer layer for efficient polymer solar cells. The Journal of Physical Chemistry. 2014, 118, 9309-9317

(49) Meiss J.; Uhrich C.; Fehse K.; Pfuetzner S.; Riede M. K.; Leo K.; Transparent electrode materials for solar cells. Proceedings of SPIE – The International Society for Optical Engineering. 2008, 700215

(50) Kim H.; Gilmore C. M.; Pique A.; Horwitz J. S.; Mattoussi H.; Murata H.; Kafafi Z. H.; Chrisey D.B.; Electrical, optical and structural properties of indium-tin-oxide thin films for organic light-emitting devices. Journal of Applied Physics. 1999, 86, 6451

(51) Glatthaar M.; Niggemann M.; Zimmermann B.; Lewer P.; Riede M.; Hinsch A.; Luther J.; Organic solar cells using inverted layer sequence. Thin Solid Films. 2005, 491, 298-300

(52) Huang J.; Miller P. F.; de Mello J. C.; de Mello A. J.; Bradley D. D. C.; Influence of thermal treatment on the conductivity and morphology of PEDOT/PSS films. Synthetic Metals. 2003, 139, 569-572

(53) Tvingstedt K.; Inganaes O.; Electrode grids for ITO-free organic photovoltaic devices. Adv. Mater. 2007, 19, 2893-2897

(54) Chen Yi.-H.; Lin L.-Y.; Lu C.-W.; Lin F.; Huang Z.-Y.; Lin H.-W.; Wang P.-H.; Liu Y.-H.; Wong K.-T.; Wen J.; Miller D. J.; Darling S. B.; Vacuum-deposited small-molecule organic solar cells with high power conversion efficiencies by judicious molecular design and device optimization. J. Am. Chem. Soc. 2012, 134, 13616-13623

(55) Hou W.; Xiao Y.; Han G.; Lin J.-Y.; The application of polymers in solar cells: a review. Polymers. 2019, 11, 143

(56) Leach S.; Vervloet M.; Despres A.; Breheret E.; Hare J. P.; Dennis T. J.; Kroto H. W.; Taylor R.; Walton D. R. M.; Electronic spectra and transition s of the fullerene C60. Chemical Physics, 160, 451-466

(57) Xie Q.; Perez-Cordero E.; Echegoyen L.; Electrochemical detection of C606- and C706-: enhanced stability of fullerides in solution. J. Am. Chem. Soc. 1992, 114, 3978-3980

(58) Ruoff R. S.; Tse D. S.; Malhotra R.; Lorents D. C.; Solubility of fullerene (C6) in a variety of solvents. The Journal of Physical Chemistry. 1993, 97, 3379-3383

(59) Hummelen J. C.; Knight B. W.; LePeq F.; Wudl F.; Yao J.; Wilkins C. L.; Preperation and characterization of fulleroid and methanofullerene derivatives. J. Org. Chem. 1995, 60, 532-538

(60) He Y.; Chen H.-Y.; Hou J.; Li Y.; Indene-C60 bisadduct: a new acceptor for high-performance polymer solar cells. 2010, 132, 1377-1382

(61) Dominguez I. F.; Distler A.; Lüer L.; Stability of organic solar cells: the influence of nanostructured carbon materials. Advanced Energy Materials. 2016, 7, 1601320

(62) Distler A.; Sauermann T.; Egelhaaf H.-J.; Rodman S.; Waller D.; Cheon K.-S.; Lee M.; Guldi D. M.; The effect of PCBM dimerization on the performance of bulk heterojunction solar cells. Advanced Energy Materials. 2013, 4 1300693

(63) Yan C.; Barlow S.; Wang Z.; Yan H.; Jen A. K.-Y.; Marder S. R.; Zhan X.; Non-fullerene acceptors for organic solar cells. Nature Review Materials. 2018, 3, 18003

(64) Dennler G.; Scharber M. C.; Brabec C. J.; Polymer-Fullerene Bulk-Heterojunction Solar Cells Adv. Mater. 2009, 21, 1323–38

(65) Kozma E.; Catellani M.; Perylene diimides based materials for organic solar cells Dye. Pigment. 2013, 98, 160–79

(66) Li C.; Wonneberger H.; Perylene imides for organic photovoltaics: yesterday, today, and tomorrow. Adv. Mater. 2012, 24, 613–36

(67) Dincalp H.; Kizilok S.; Icli S.; Fluorescent macromolecular perylene diimides containing pyrene or indole units in bay positions. Dyes and Pigments. 2010, 86, 32-41

(68) Huang C.; Barlow S.; Marder S. R.; Perylene-3,4,9,10-tetracarboxylic acid diimides: synthesis, physical properties, and use in organic electronics. J. Org. Chem. 2011, 76, 2386-2407

(69) Sun H.; Chen F.; Chen Z.-K.; Recent progress on non-fullerene acceptors for organic photovoltaics. Materials Today. 2019, 24, 94-118

(70) Zhao J.; Li Y.; Lin H.; Yuhang L.; High-efficiency non-fullerene organic solar cells enabled by a difluorobenzothiadizole-based donor polymer combined with a properly matched small molecule acceptor. Energy & Environmental Science. 2014, 8, 520-525

(71) Guo Y.; Li Y.; Awartani O. M.; Zhao J.; A vinylene-bridged perylenediimide-based polymeric acceptor enabling efficient all-polymer solar cells processed under ambient conditions. Advanced Materials. 2016, 28

(72) Li G.; Yang W.; Wang S.; Liu T.; Yan C.; Li G.; Zhang Y.; Li D.; Wang X.; Hao P.; Li J.; Huo L.; Yan H.; Tang B.; Methane-perylene diimide based small molecule acceptors for high efficiency non-fullerene organic solar cells. J. Mater. Chem. C. 2019, 7, 10901-10907

(73) Li M.; Wang H.; Liu Y.; Zhou Y.; Lu H.; Song J.; Bo Z.; Perylene diimide acceptor with two planar arms and a twisted core for high efficiency polymer solar cells. Dyes and Pigments. 2020, 108186

(74) Qureshi M. B. A.; Li M.; Wang H.; Song J.; Bo Z.; Nonfullerene acceptors with an N-annulated perylene core and two perylene diimide units for efficient organic solar cells. Dyes and Pigments. 2020, 173, 107970

(75) Luo Z.; Liu T.; Chen Z.; Xiao Y.; Zhang G.; Huo L.; Zhong C.; Lu X.; Yan H.; Sun Y.; Yang C.; Isomerization of perylene diimide based acceptors enabling high-performance nonfullerene organic solar cells with excellent fill factor. Advanced Science. 2019, 6, 1802065

(76) Li G.; Yang S.; Liu T.; Li J.; Yang W.; Luo Z.; Yan C.; Li D.; Wang X.; Cui G.; Yang T.; Xu L.; Zhan S.-Z.; Huo L.; Yan H.; Tang B.; Functionalizing tetraphenylpyrazine with perylene diimides (PDIs) as high-performance nonfullerene acceptors. J. Mater. Chem. C. 2019, 7, 14563-13570

(77) Sharma V.; Kovida; Sahoo D.; Varghese N.; Mohanta K.; Koner A. L.; Synthesis and photovoltaic application of NIR-emitting perylene-monoimide dyes with large Stokes-shift. RSC Advances. 2019, 9, 30448-30452

(78) Jones B. A.; Facchetti A.; Wasielewski Mi. R.; Marks T. J.; Tuning orbital energetics in arylene diimide semiconductors. Materials design for ambient stability of n-tape charge transport. J. Am. Chem. Soc. 2007, 129, 15259-15278

(79) Lin Z.; Li C.; Meng D.; Li Y.; Wang Z.; Hybrid corannulene-perylene dyes: facile synthesis and optoelectronic properties. Chemistry An Asian Journal. 2016, 11, 2695-2699

(80) Würthner F.; Osswald P.; Schmidt R.; Kaiser T. E.; Mansikkamäki H.; Könemann M.; Synthesis and optical and electrochemical properties of core-fluorinated perylene bisimides. Org. Lett., 2006, 8, 3765-3768

(81) Fluoreszenzorange. https://www.kremer-pigmente.com/media/pdf/94738.pdf (accessed Jan 21, 2020)

(82) Brixi S.; Melville O. A.; Boileau N.; Lessard B. H.; The influence of air and temperature on the performance of PBDB-T and P3HT in organic thin film transistors. J. Mater. Chem. C. 2018, 6, 11972-11979

8 Appendix

8.1 List of Figures

8.2 List of Tables

8.3 List of Abbreviations

AIL	Anode Interfacial Layers
CIL	Cathode Interfacial Layers
DCM	Dichloromethane
DFT	Density Funtional Theory
EQE	External Quantum Efficiency
EtOH	Ethanol
HOMO	Highest Occupied Molecular Orbital
ITIC	3,9-bis(2-methylene-(3-(1,1-dicyanomethylene)-indanone))-5,5,11,11-tetrakis(4-hexylphenyl)-dithieno[2,3-d:2',3'-d']-s-indaceno[1,2-b:5,6-b']dithiophene
ITIC-F	3,9-bis(2-methylene-((3-(1,1-dicyanomethylene)-6,7-difluoro)-indanone))-5,5,11,11-tetrakis(4-hexylphenyl)-dithieno[2,3-d:2',3'-d']-s-indaceno[1,2-b:5,6-b']dithiophene
LUMO	Lowest Unoccupied Moleculra Orbital
MeOH	Methanol
MS	Mass Spectrometry
NMR	Nuclear Magnetic Resonance
PBDB-T/PCE12	Poly[(2,6-(4,8-bis(5-(2-ethylhexyl)thiophen-2-yl)-benzo[1,2-b:4,5-b']dithiophene))-alt-(5,5-(1',3'-di-2-thienyl-5',7'-bis(2-ethylhexyl)benzo[1',2'-c:4',5'-c']dithiophene-4,8-dione)]
PCBM	[6,6]-Phenyl-C61-butyric acid methyl ester
PDI	Perylenediimide
PDI-Br_2	5,12-dibromo-2,9-bis(2,6-diisopropylphenyl)anthra[2,1,9-def:6,5,10-d'e'f']diisoquinoline-1,3,8,10(2H,9H)-tetraone
PDI-$(CN)_2$	2,9-bis(2,6-diisopropylphenyl)-1,3,8,10-tetraoxo-1,2,3,8,9,10-hexahydroanthra[2,1,9-def:6,5,10-d'e'f']diisoquinoline-5,12-dicarbonitrile
PDI-F_2	2,9-bis(2,6-diisopropylphenyl)-5,12-difluoroanthra[2,1,9-def:6,5,10-d'e'f']diisoquinoline-1,3,8,10(2H,9H)- tetraone

$PDI\text{-}(PMI)_2$	2,9-bis(2,6-diisopropylphenyl)-5-(2-(2,6-diisopropylphenyl)-1,3-dioxo-2,3-dihydro-1H-benzo[10,5]anthra[2,1,9-def]isoquinolin-8-yl)-12-(2-(2,6-diisopropylphenyl)-12-methyl-1,3-dioxo-2,3-dihydro-1H-benzo[10,5]anthra[2,1,9-def]isoquinolin-8-yl)anthra[2,1,9-def:6,5,10-d'e'f']diisoquinoline-1,3,8,10(2H,9H)-tetraone
PEDOT	Poly(ethylene dioxythiophene)
PMI	Perylenemonoimide
PSS	polystyrene sulfonate
RT	Room Temperature
TGA	Thermogravimetric Analysis
TLC	Thin Layer Chromatography

8.4 Analytical Data

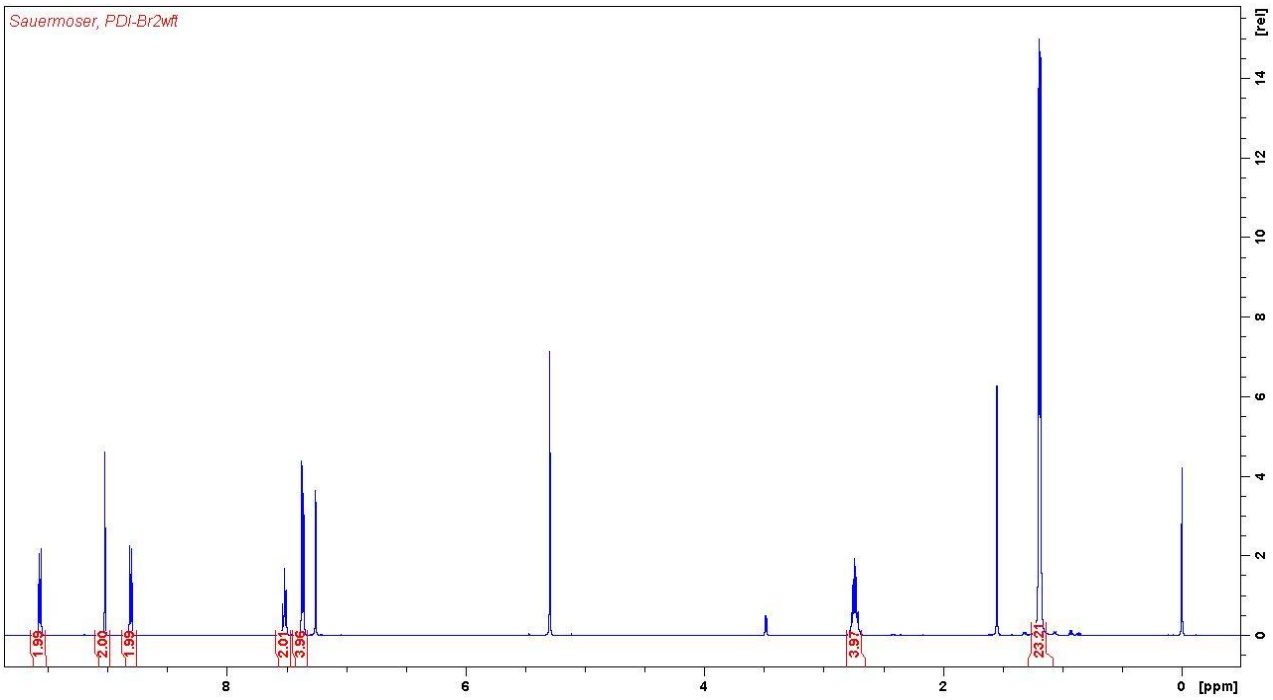

Figure 32: ^{1}H-NMR-spectra of the purified PDI-Br$_2$; solvent peak visible

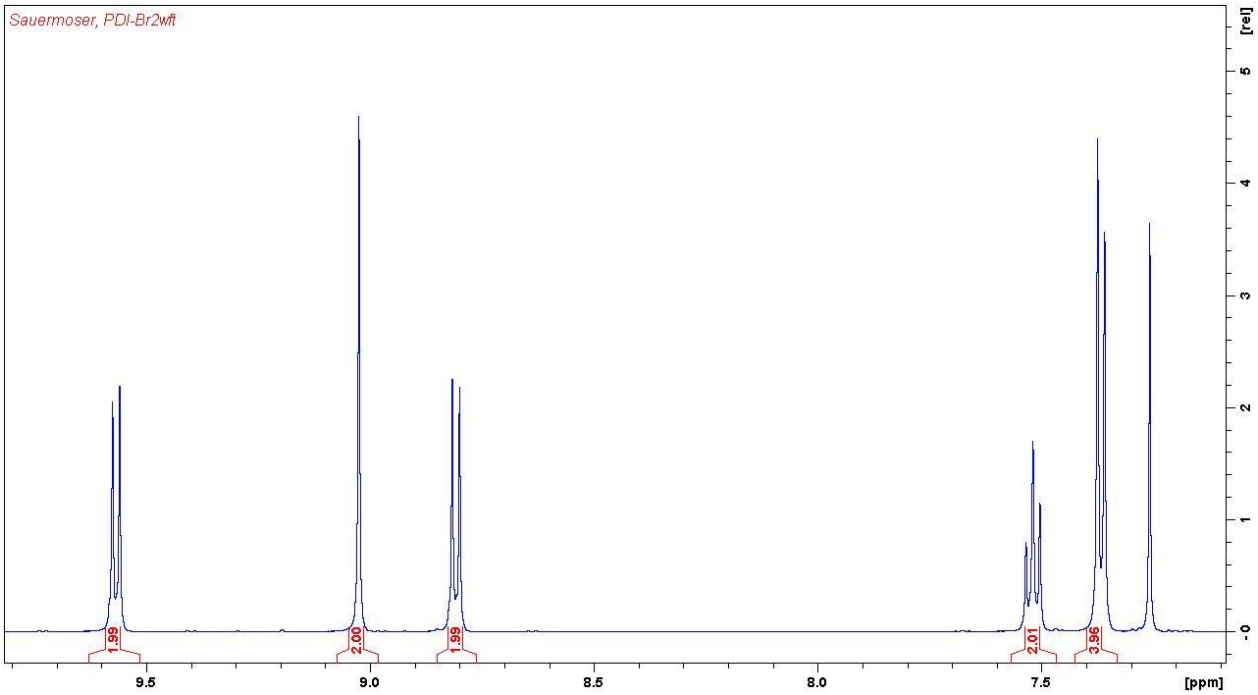

Figure 33: ^{1}H-NMR-spectra of the aromatic region of purified PDI-Br$_2$; solvent peak visible

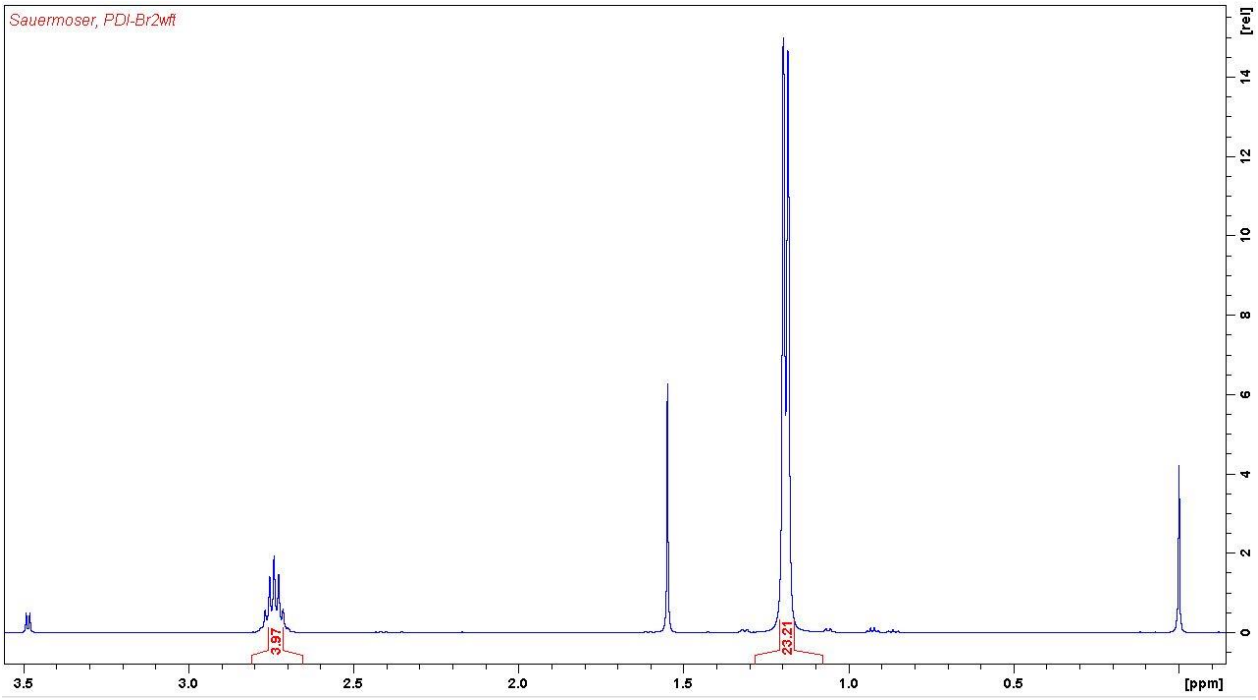

Figure 34: ^{1}H-NMR-spectra of the aliphatic region of purified PDI-Br_2; solvent peak visible

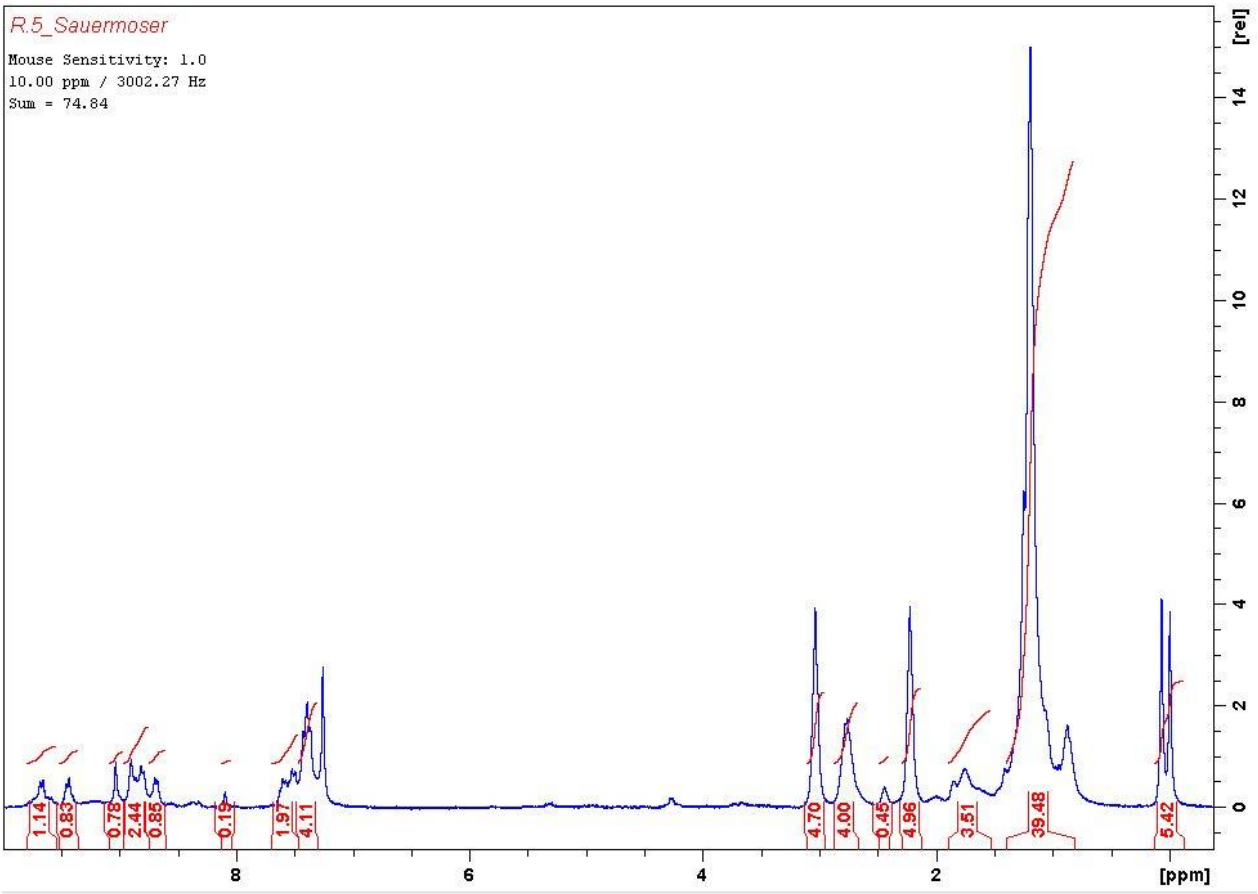

Figure 35: ^{1}H-NMR-spectra of the first reaction step for the synthesis of PDI-F_2

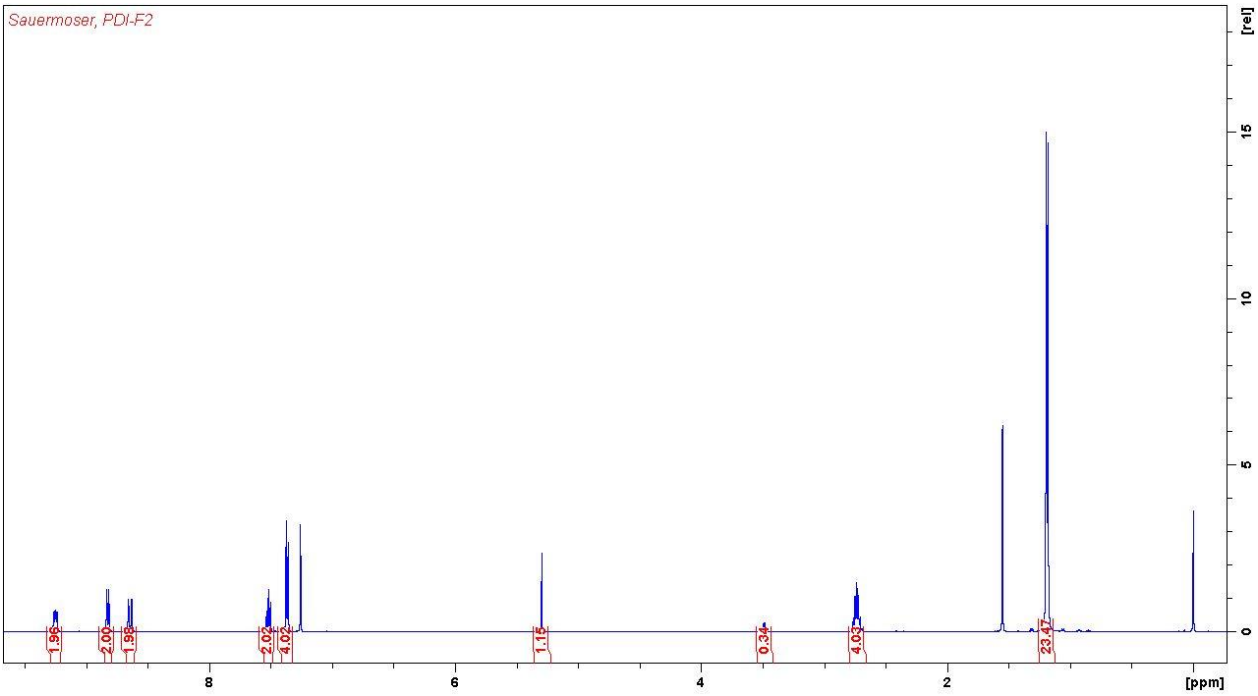

Figure 36: ^{1}H-NMR-spectra of the purified PDI-F$_2$; solvent peak visible

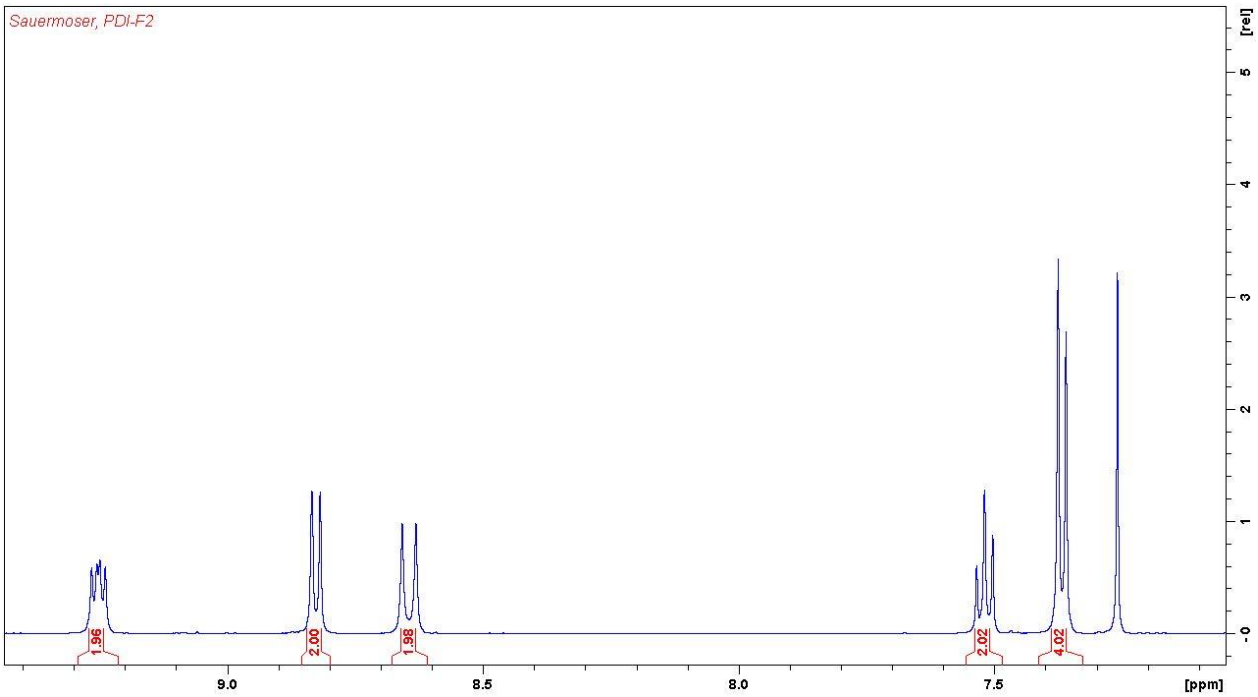

Figure 37: ^{1}H-NMR-spectra of the aromatic region of purified PDI-F$_2$; solvent peak visible

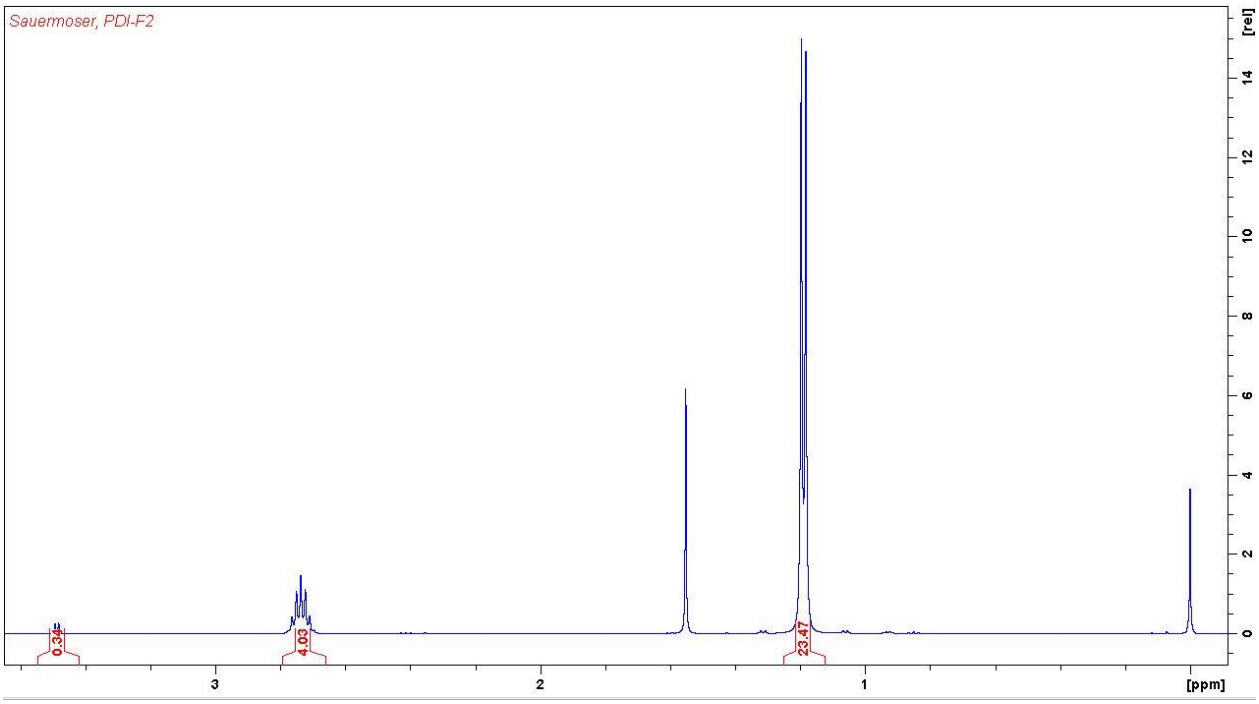

Figure 38: ^{1}H-NMR-spectra of the aliphatic region of purified PDI-F_2, solvent peak visible

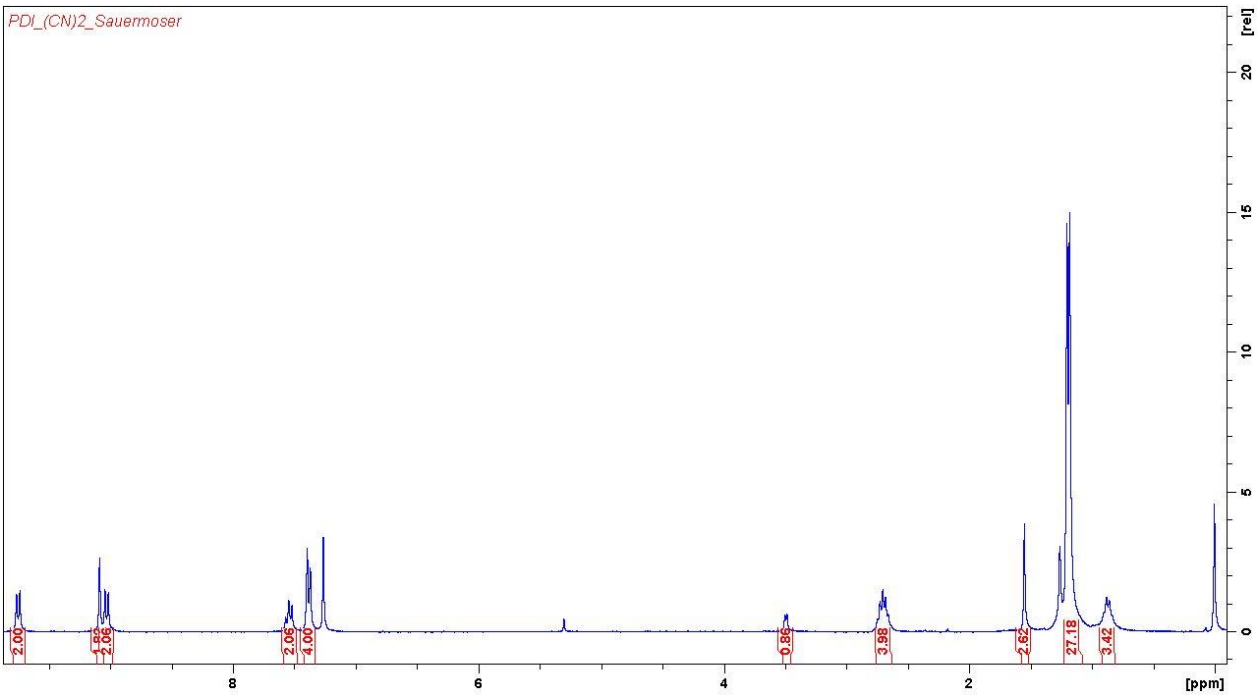

Figure 39: ^{1}H-NMR-spectra of purified PDI-$(CN)_2$; solvent peak and by-products visible

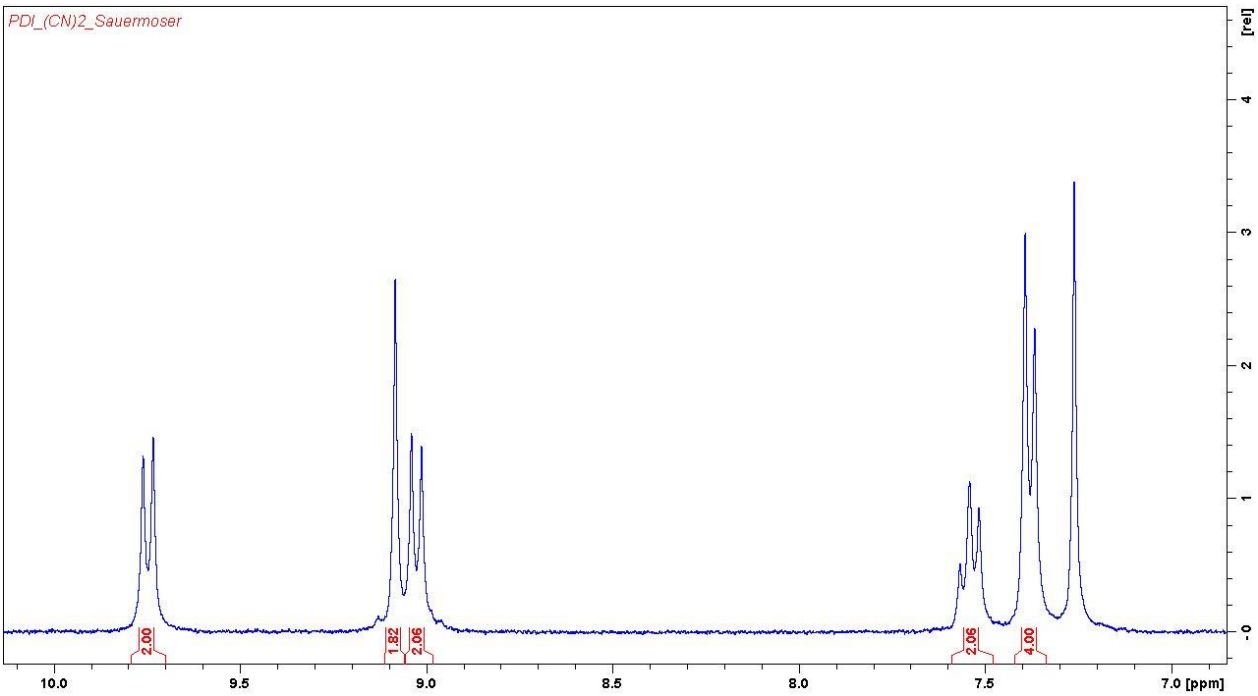

Figure 40: ^{1}H-NMR-spectra of the aromatic region of purified PDI-(CN)$_2$; solvent peak and by-products visible

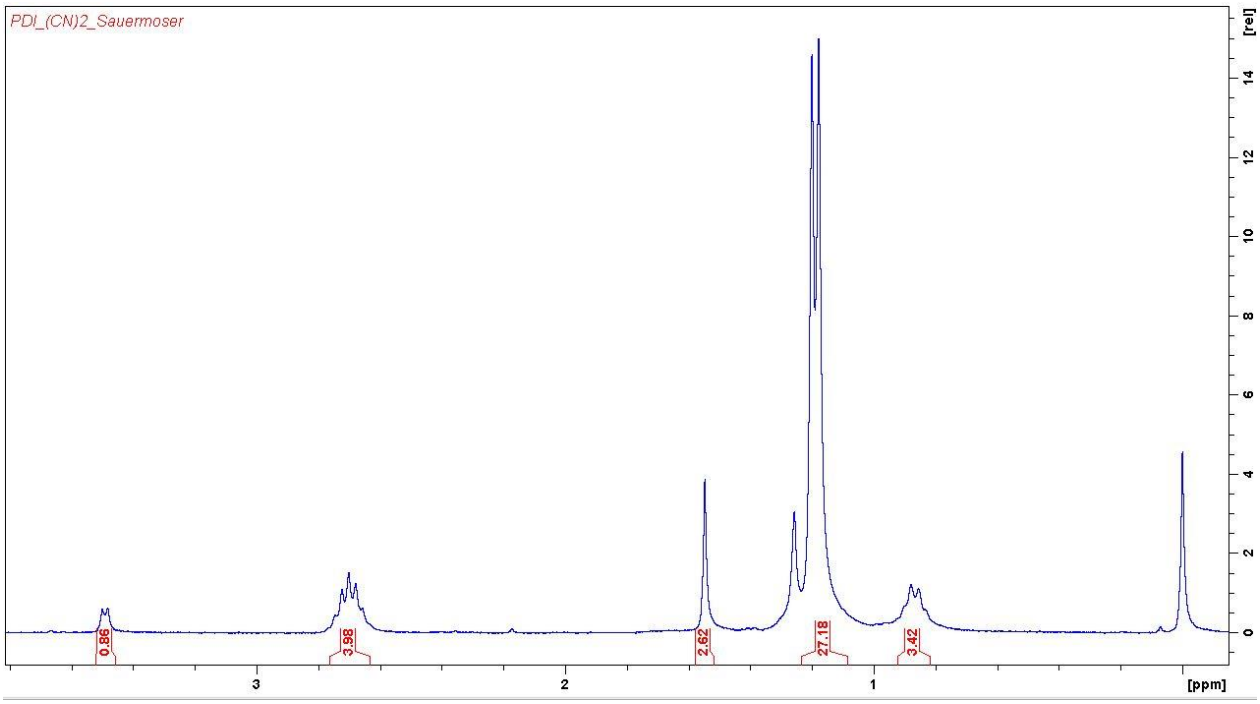

Figure 41: ^{1}H-NMR-spectra of the aliphatic region of purified PDI-(CN)$_2$; solvent peak and by-products visible

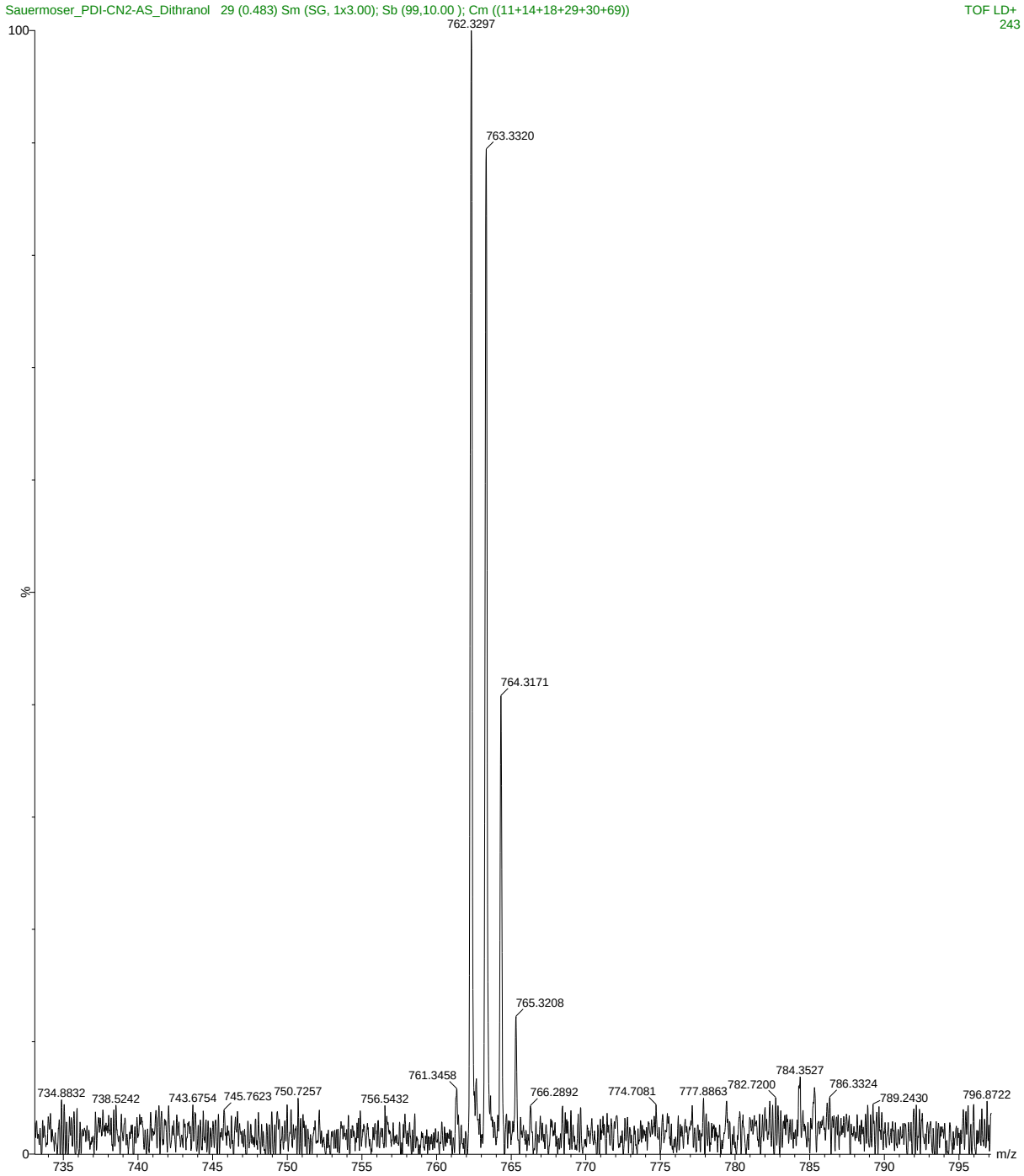

Figure 42: MS spectra of PDI-(CN)$_2$ (1)

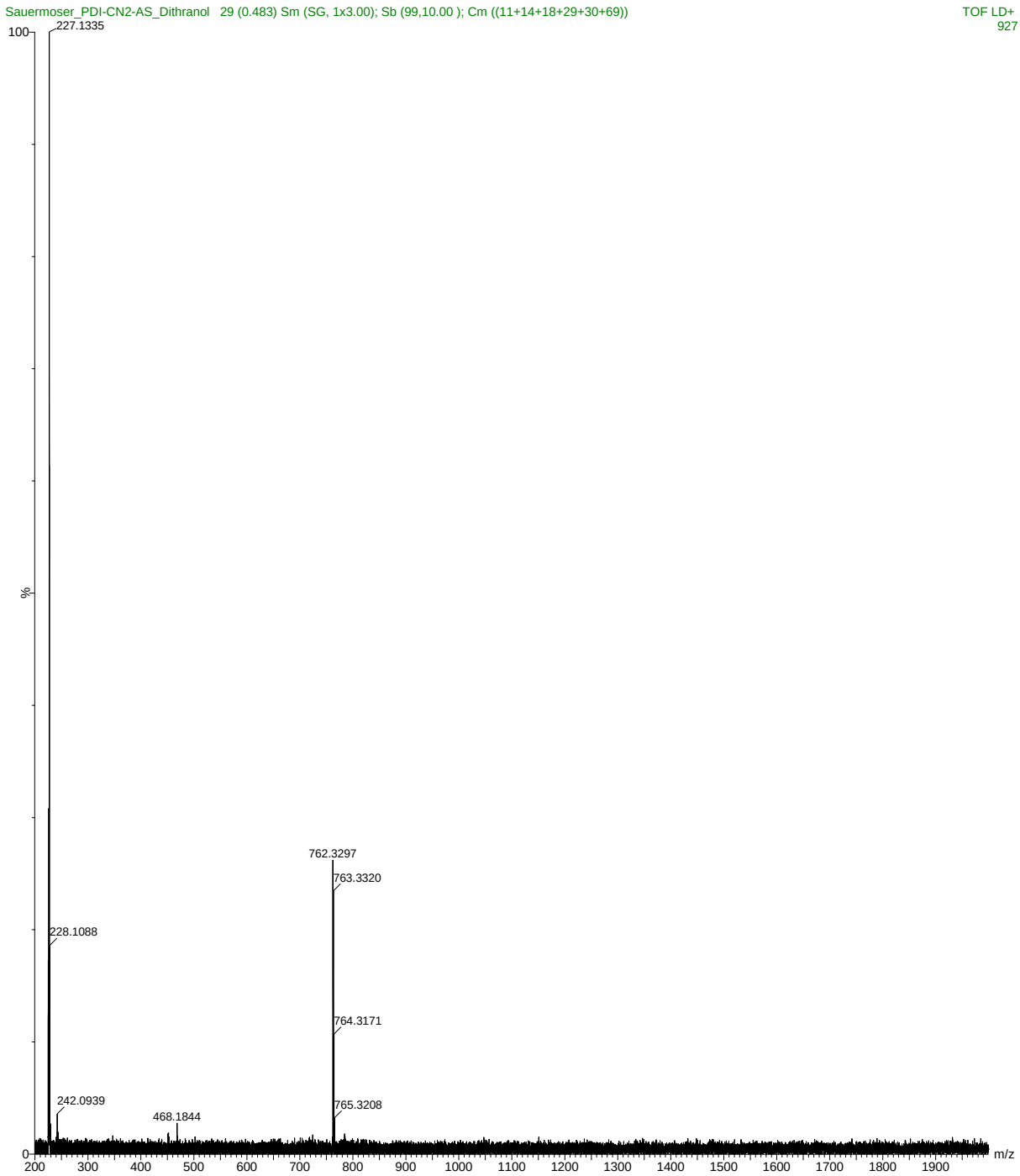

Figure 43: MS spectra of PDI-$(CN)_2$ (2)

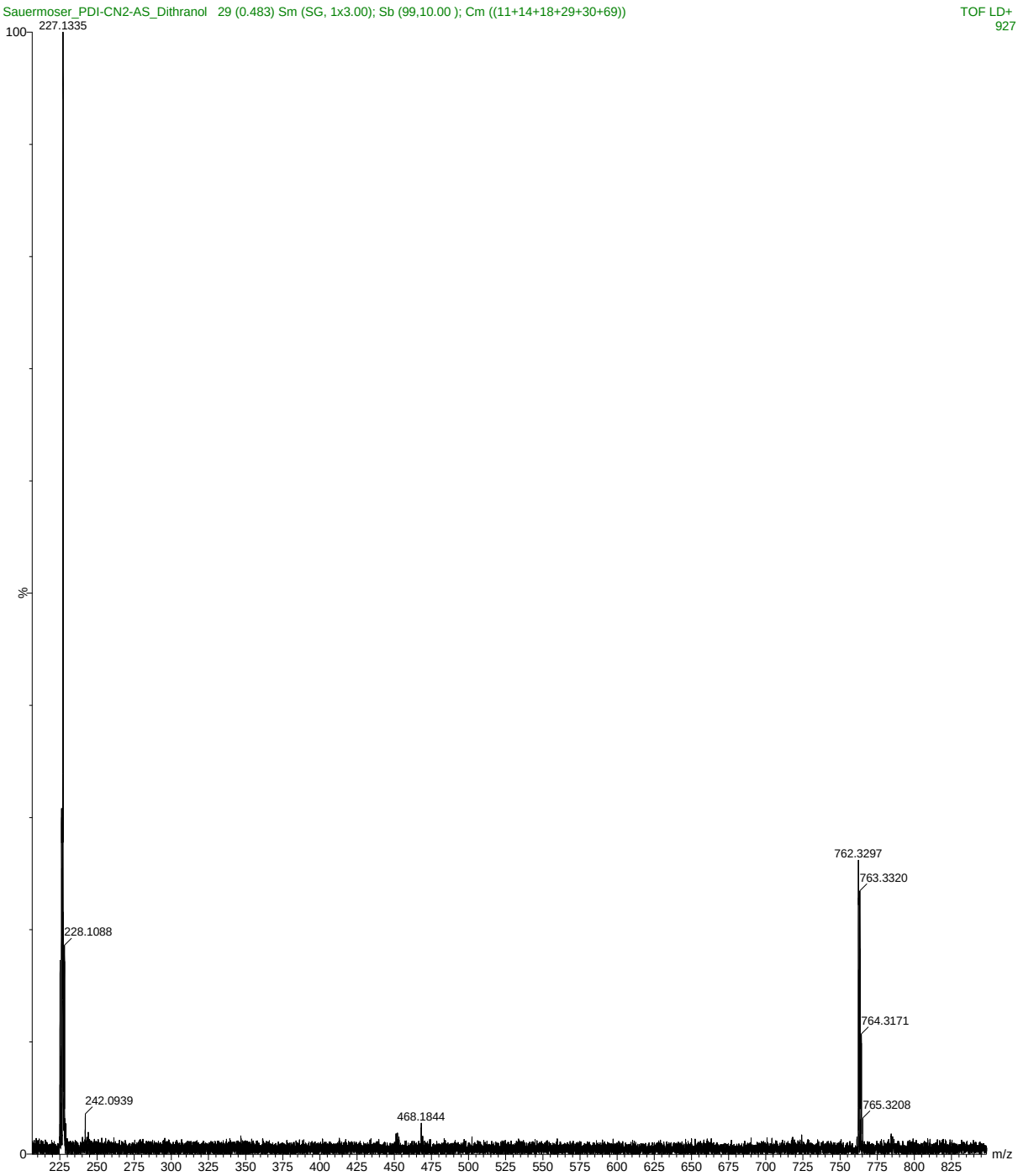

Figure 44: MS spectra of PDI-$(CN)_2$ (2)

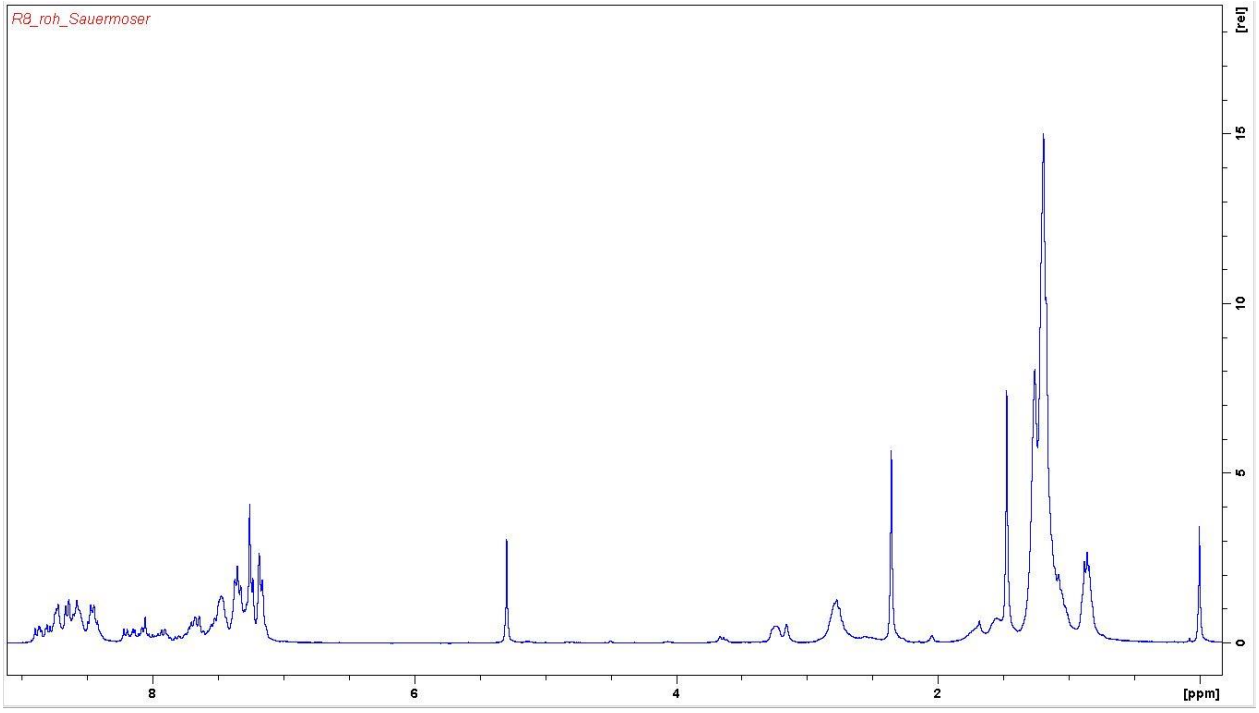

Figure 45: ^{1}H-NMR-spectra of the crude PDI-(PMI)$_2$

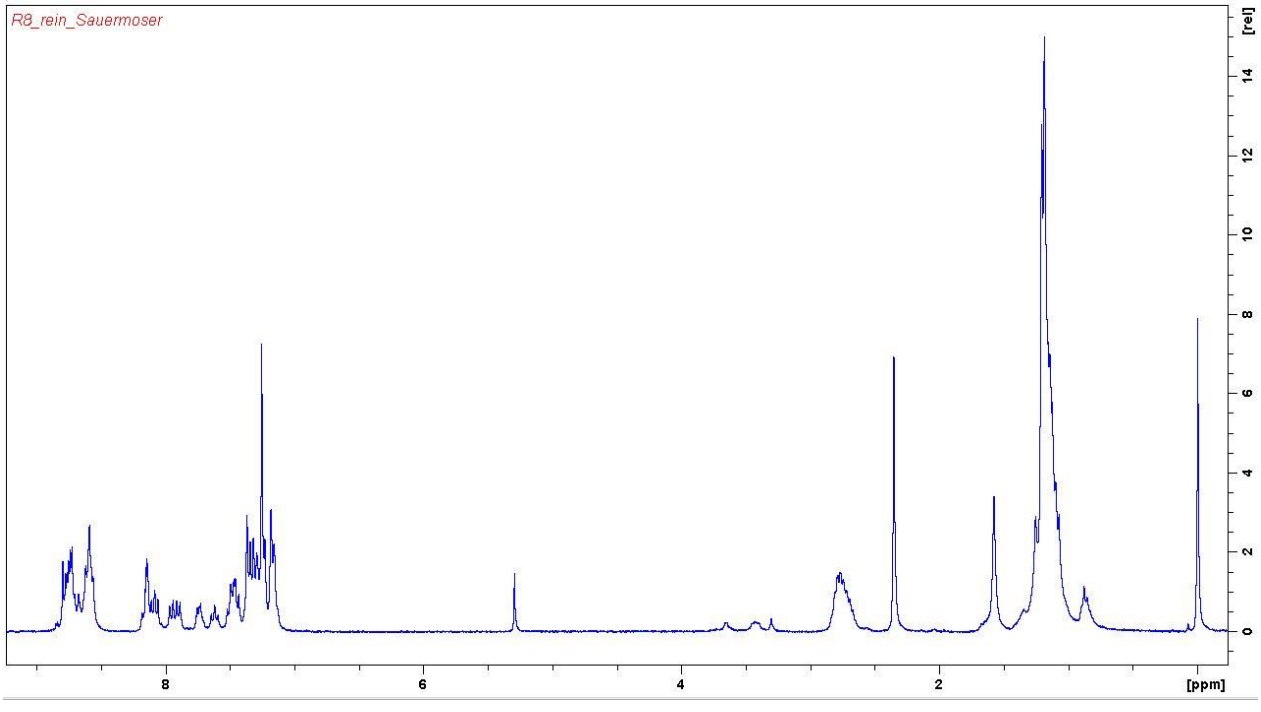

Figure 46: ^{1}H-NMR-spectra of PDI-(PMI)$_2$ after flash chromatography and recrystallization; still impurities visible